A polynuclear and two dinuclear copper(II) Schiff base complexes: Synthesis, characterization, self-assembly, magnetic property and DFT study

Anik Bhattacharyya,[a] Antonio Bauzá,[b] Stephen Sproules,[c] Louise S. Natrajan,[d] Antonio Frontera,[b,*] Shouvik Chattopadhyay[a,*]

[a]Department of Chemistry, Inorganic Section, Jadavpur University, Kolkata - 700032, India.

[b]Departament de Química, Universitat de les Illes Balears, Crta. de Valldemossa km 7.5, 07122 Palma (Baleares), Spain.

[c]WestCHEM, School of Chemistry, University of Glasgow, Glasgow G12 8QQ, United Kingdom.

[d]School of Chemistry, The University of Manchester, Oxford Road, Manchester M13 9PL, United Kingdom

e-mail: shouvik.chem@gmail.com Tel: +(91)33-2457-2941

Abstract: Three elongated (4+1) square pyramidal copper(II) complexes, $[Cu_2(L)_2(\mu_{1,1}\text{-}N_3)_2]\cdot H_2O$ (**1**), $[Cu_2(L)_2(\mu_{1,1}\text{-}NCO)_2]$ (**2**) and $[Cu(L)(\mu_{1,5}\text{-}dca)]_n$ (**3**) [HL = 1((2-(methylamino)ethylimino)methyl)naphthalen-2-ol and dca = dicyanamide], have been synthesized using a tridentate N_2O donor Schiff base ligand (HL) and characterized. Complexes **1** and **2** are centrosymmetric dimers in which copper(II) centres are connected by asymmetric double end on pseudohalide bridges. Complex **3** features a 1D zigzag chain in which copper(II) centres are connected by end to end dca bridges. Variable temperature (2-300K) magnetic susceptibility measurements indicate the presence of antiferromagnetic exchange coupling between copper(II) centres in complexes **1** (J = -2.313 cm^{-1}) and **3** (J = -0.344 cm^{-1}), whereas complex **2** shows ferromagnetic exchange coupling between copper(II) centres (J = 0.513 cm^{-1}). DFT calculations also corroborate the data. The fluid solution EPR spectra recorded at 293 K are typical of copper(II) species. Significant supramolecular interactions are explored using high level DFT calculations (BP86-D3/def2-TZVP) and characterized by Bader's theory of "atoms-in-molecules".

1. Introduction

A rich variety of architectures of coordination complexes could be produced by linking transition metal centres with bridging ligands [1-6]. These coordination complexes could have potential applications in molecular based ferromagnets, non-linear optics and ferroelectrics [7-9]. A variety of bridging groups have been employed for the synthesis of such coordination complexes. Among them pseudohalide (azide, cyanate, thiocyanate, dicyanamide etc.) bridged complexes of transition metals have attracted the attention of coordination chemists for their potential application in bioinorganic modelling chemistry [10], magnetic materials [11-12] and catalysis [13]. Several N_2O donor Schiff bases are popularly used as blocking ligands in preparing such complexes [14-17]. Focusing on copper(II), pseudohalides have widely been employed for the syntheses of such complexes because of their ability to coordinate copper(II) in different modes [18-22]. Both basal-basal and basal-apical modes are observed in the binding of adjacent copper(II) centres by end on pseudohalides [23]. Basal-basal bridging mode of end on pseudohalides may impose ferromagnetic or antiferromagnetic coupling between adjacent copper(II) centres depending on Cu-N-Cu angle [23]. On the other hand, due to the absence of any meaningful overlap between magnetic orbitals, basal-apical bridges usually give rise to very small magnetic couplings for end on modes [24-31]. Same is the case for the end to end dca bridged complexes due to relatively longer distance between the copper(II) centres [32-33]. However, such complexes could be used to explore the energy associated with various non-covalent interactions [34-50], forming interesting supramolecular networks with different sizes and shapes.

In the present work, we have synthesized two dinuclear asymmetric double end on pseudo-halide bridged and a polynuclear end to end dca bridged copper(II) complexes, $[Cu_2(L)_2(\mu_{1,1}\text{-}N_3)_2]\cdot H_2O$ (**1**), $[Cu_2(L)_2(\mu_{1,1}\text{-}NCO)_2]$ (**2**) and $[Cu(L)(\mu_{1,5}\text{-}dca)]_n$ (**3**) [HL = a tridentate N_2O donor Schiff base, 1((2-

(methylamino)ethylimino)methyl)naphthalen-2-ol]. Herein, we would like to report the synthesis, spectroscopic characterizations, crystal structures, magnetic properties and supramolecular assemblies of these three complexes. Moreover, DFT calculations have been employed to obtain a better understanding of the magnetic exchange mechanism and to calculate energies associated with different supramolecular interactions.

2. Experimental Section

All chemicals were of reagent grade and used as purchased from Sigma-Aldrich without further purification.

Caution!!! Although no problems were encountered in this work, organic ligands in presence of azides are potentially explosive. Only a small amount of the material should be prepared and it should be handled with care.

2.1 Preparations

2.1.1 Preparation of $[Cu_2(L)_2(\mu_{1,1}\text{-}N_3)_2]\cdot H_2O$ ***(1)***

A methanol solution of N-methyl-1,2-diaminoethane (0.10 mL, 1 mmol) and 2-hydroxy-1-naphthaldehyde (172 mg, 1 mmol) was refluxed for ca. 1 h to form the tridentate Schiff base ligand, HL. The ligand was not isolated. A methanol (10 mL) solution of copper(II) acetate monohydrate (200 mg, 1 mmol) was added into the methanol solution of the ligand HL to get a dark blue solution. A methanol-water solution of sodium azide (65 mg, 1 mmol) was added into the reaction mixture with constant stirring. The stirring was continued for an additional ca. 2 h. Dark green single crystals,

suitable for X-ray diffraction, were obtained after few days by slow evaporation of the solution in open atmosphere.

Yield: 263 mg [77%, based on copper (II)]; Anal. Calc. for $C_{28}H_{32}Cu_2N_{10}O_3$ (683.74): C, 50.52; H, 4.54; N, 21.04 %. Found: C, 50.3; H, 4.3; N, 21.2 %. FT-IR (KBr, cm^{-1}): 3361 (ν_{NH}), 2033 (ν_{N3}), 1617 ($\nu_{C=N}$); UV-Vis, λ_{max} (nm) [ε_{max}($Lmol^{-1}cm^{-1}$)] (acetonitrile): 311 (1.4×10^4), 382 (1.23×10^4), 589 (2.57×10^2).

*2.1.2 Preparation of $[Cu_2(L)_2(\mu_{1,1}\text{-}NCO)_2]$ (**2**)*

It was prepared in a similar method as that of complex **1**, except that sodium cyanate (65 mg, 1 mmol) was used instead of sodium azide. Single crystals, suitable for X-ray diffraction, were obtained on slow evaporation of the solution.

Yield: 276 mg [83%, based on copper (II)]; Anal. Calc. for $C_{30}H_{30}Cu_2N_6O_4$ (665.70): C, 54.13; H, 4.54; N, 12.62 %. Found: C, 53.9; H, 4.3; N, 12.8 %. FT-IR (KBr, cm^{-1}): 3377 (ν_{NH}), 2215 (ν_{NCO}), 1621 ($\nu_{C=N}$); UV-Vis, λ_{max} (nm) [ε_{max}($Lmol^{-1}cm^{-1}$)] (acetonitrile): 314 (1.53×10^4), 393 (1.17×10^4), 592 (2.33×10^2).

*2.1.3 Preparation of $[Cu(L)(\mu_{1,5}\text{-}dca)]_n$ (**3**)*

It was also prepared in a similar method as that of complex **1**, except that sodium dicyanamide (89 mg, 1 mmol) was used instead of sodium azide. Suitable single crystals for X-ray diffraction were obtained on slow evaporation of the solution in open atmosphere.

Yield: 261 mg [73%, based on copper (II)]; Anal. Calc. for $C_{16}H_{15}CuN_5O$ (356.88): C, 53.85; H, 4.24; N, 19.62 %. Found: C, 53.6; H, 4.1; N, 19.8 %. FT-IR (KBr, cm^{-1}): 3367 (ν_{NH}), 2178, 2232, 2287 ($\nu_{N(CN)2}$), 1619 ($\nu_{C=N}$); UV-Vis, λ_{max} (nm) [ε_{max}($Lmol^{-1}cm^{-1}$)] (acetonitrile): 307 (1.44×10^4), 387 (1.22×10^4), 597 (2.41×10^2).

2.2 Physical measurements

Elemental analyses (carbon, hydrogen and nitrogen) were performed using a PerkinElmer 240C elemental analyzer. IR spectra in KBr (4500-500 cm^{-1}) were recorded with a PerkinElmer Spectrum Two spectrophotometer. Electronic spectra in acetonitrile were recorded on a PerkinElmer Lambda 35 UV-visible spectrophotometer. Magnetic data were recorded using a SQUID magnetometer (Quantum Design MPMS-XL) over a temperature range of 2-300 K in a 1 T external field. Corrections for diamagnetism were made using Pascal's constants and magnetic data were corrected for diamagnetic contributions from the sample holder. Fits were performed using the program JulX. X-band EPR spectra were recorded on a Bruker ELEXSYS E500 spectrometer at 293 K and simulations performed using Bruker's Xsophe Program Package [51]. Powder X-ray diffraction was performed on a Bruker D8 instrument with Cu K_α radiation. High resolution mass spectroscopy was performed on a Waters Xevo G2 QTOf mass spectrometer.

2.3 X-ray crystallography

Suitable single crystals of each complex were used for data collection using a 'Bruker SMART APEX II' diffractometer equipped with graphite monochromated Mo K_α radiation (λ = 0.71073 Å) at 100 K. The molecular structures were solved by direct method and refined by full-matrix least squares on F^2 using the SHELX-97 package [52-53]. Non-hydrogen atoms were refined with anisotropic thermal parameters. The hydrogen atoms attached to oxygen and nitrogen atoms were located by difference Fourier maps and were kept at fixed positions. All other hydrogen atoms were placed in their geometrically idealized positions and constrained to ride on their parent atoms. Multi-scan empirical absorption corrections were applied to the data using the program SADABS [54].

Details of crystallographic data and refinements are given in Table 1. CCDC reference numbers are 1053629-1053631 for **1**, **2** and **3** respectively.

2.4 Theoretical calculations for supramolecular assembly

All calculations were carried out using the TURBOMOLE version 7.0 [55] using the BP86-D3/def2-TZVP level of theory. To evaluate the interactions in the solid state, we have used the crystallographic coordinates. This procedure and level of theory have been successfully used to evaluate similar interactions [56-59]. The interaction energies were computed by calculating the difference between the energies of isolated monomers and their assembly. The interaction energies were corrected for the Basis Set Superposition Error (BSSE) using the counterpoise method [60]. The "atoms-in-molecules" (AIM) [61] analysis was performed at the BP86-D3/def2-TZVP level of theory. The calculation of AIM properties was done using the AIMAll program [62].

2.5 Theoretical calculations for magnetic properties

The magnetic coupling constants are described using the Heisenberg model. The hybrid B3LYP functional [63-65] has been used in all calculations as implemented in Gaussian-09 [66] using the 6-31+G* basis set for all atoms. The approach used in this work to determine the exchange coupling constants for dinuclear complexes has been described before in the literature [67-70].

2.6 Hirshfeld surfaces

Hirshfeld surfaces [71-73] and the associated 2D-fingerprint [74-76] plots were calculated using Crystal Explorer [77] which accepted a structure input file in CIF format. Bond lengths to hydrogen atoms were set to standard values. For each point on the Hirshfeld isosurface, two distances d_e, the distance from the point to the nearest nucleus external to the surface and d_i, the

distance to the nearest nucleus internal to the surface, were defined. The normalized contact distance (d_{norm}) based on d_e and d_i was given by

$$d_{norm} = \frac{(\mathrm{d_i} - \mathrm{r_i^{vdw}})}{\mathrm{r_i^{vdw}}} + \frac{(\mathrm{d_e} - \mathrm{r_e^{vdw}})}{\mathrm{r_e^{vdw}}}$$

where r_i^{vdw} and r_e^{vdw} were the van der Waals radii of the atoms. The value of d_{norm} was negative or positive depending on intermolecular contacts, being shorter or longer than the van der Waals separations. The parameter d_{norm} displayed a surface with a red-white-blue color scheme, where bright red spots highlighted shorter contacts, white areas represented contacts around the van der Waals separation, and blue regions were devoid of close contacts. For a given crystal structure and set of spherical atomic electron densities, the Hirshfeld surface was unique [78] and it was this property that suggested the possibility of gaining additional insight into the intermolecular interaction of molecular crystals.

3. Results and discussion

3.1 Synthesis

The tridentate N_2O donor Schiff base ligand (HL) has been produced by the condensation of N-methyl-1,2-diaminoethane and 2-hydroxy-1-naphthaldehyde following the literature method [79]. This Schiff base (HL) on reaction with copper(II) acetate monohydrate and different pseudohalides gives three copper(II) complexes $[Cu_2(L)_2(\mu_{1,1}\text{-}N_3)_2]\cdot H_2O$ (**1**), $[Cu_2(L)_2(\mu_{1,1}\text{-}NCO)_2]$ (**2**) and $[Cu(L)(\mu_{1,5}\text{-}dca)]_n$ (**3**). The reaction with azide and cyanate produces double end on bridged copper(II) dimers whereas use of dicyanamide leads to the formation of an end to end dicyanamide bridged zigzag polymer. Formation of all complexes is shown in Scheme 1.

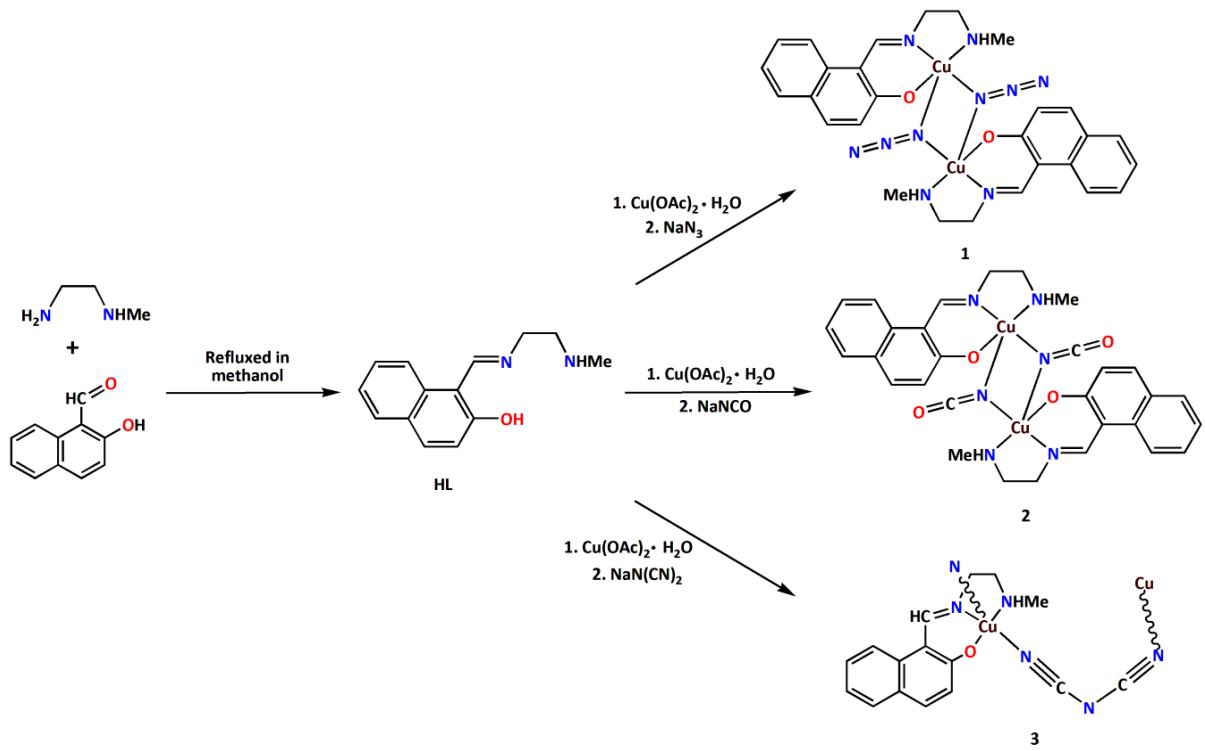

Scheme 1: Synthetic route to complexes.

3.2 Description of structures

*3.2.1 Complexes $[Cu_2(L)_2(\mu_{1,1}\text{-}N_3)_2]\cdot H_2O$ (**1**) and $[Cu_2(L)_2(\mu_{1,1}\text{-}NCO)_2]$ (**2**)*

Complexes **1** and **2** crystallize in the monoclinic space group *C2/c* and triclinic space group *P-1*, respectively. Perspective views of **1** and **2** with selective atom numbering schemes are shown in Figures 1 and 2. Selected bond lengths and angles are gathered in Table 2. Both complexes are centrosymmetric dimers in which copper(II) centres are connected by two end on bridging anionic ligands, azide in **1** and cyanate in **2**. Each copper(II) centre shows a five-coordinated elongated (4 + 1) square pyramidal environment where three donor atoms of the tridentate N_2O Schiff base and one anionic ligand (azide in **1** and cyanate in **2**) occupy the basal plane. On the other hand, another anionic ligand (azide in **1** and cyanate in **2**) occupies the apical site. Each azide ion bridges copper(II) centres

in end on basal-apical fashion. The double end on azide bridging in these complexes lead to a perfectly planar Cu_2N_2 ring as these dinuclear complexes sits on a crystallographic inversion centre with a Cu–N–Cu bond angle of 95.5(2)° in **1** and 88.4(1)° in **2**. The bond lengths in the equatorial plane are very similar in both complexes. The Cu–N_{imine} distances are significantly shorter (1.936(4) Å for **1** and 1.922(3) Å for **2**) than the Cu–N_{amine} distances (2.028(5) Å for **1** and 2.036(4) Å for **2**), as also observed in similar complexes [80-81]. The copper(II)-nitrogen(anion) bond lengths in the equatorial plane range from 1.937(4)-1.979(5) Å, while the copper(II)-nitrogen(anion) axial bond lengths range from 2.442(5)-2.692(4) Å. The bridging pseudohalides are quasi-linear with the N–N–N angle being 178.2(6)° in **1** and N–C–O angle being 175.8(5)° in **2**. The intra dimer Cu···Cu distance is 3.2869(9) Å in **1** and 3.2715(8) Å in **2**.

In both complexes, the copper(II) centres assume square pyramidal geometry with Addison parameters [82] 0.06 in **1** and 0.0015 in **2**. As usual for square pyramidal structures, copper(II) centres are slightly pulled out of the mean square planes towards the apical donor atoms at distances of -0.0980(6) Å in **1** and -0.0002(5) Å in **2**. Deviations of the coordinating atoms, N(1), N(2), O(1) and N(3), from the least-square basal planes are 0.026(4), -0.028(4), 0.027(4) and -0.025(4) Å respectively in **1** and are 0.135(4), -0.140(3), 0.135(3), and -0.130(4) Å respectively in **2**. The five membered chelate ring Cu(1)–N(1)–C(2)–C(3)–N(2) in **1** assumes an intermediate conformation between half-chair and envelope being twisted on N(1)-C(2) with puckering parameters [83-85] q(2) = 0.343(7) Å and ϕ(2) = 238.7(9)°. The same ring in **2** assumes intermediate conformation between half-chair and envelope being twisted on C(2)-C(3) with puckering parameters [83-85] q(2) = 0.409(5) Å and ϕ(2) = 262.9(5)°.

The hydrogen atom, H(1), attached to the amine nitrogen atom, N(1), of complex **1** is involved in intermolecular hydrogen bonding interactions with the symmetry related (^{d} = x,-y,-1/2+z) azide

nitrogen atom N(5)^{d} to form a chain along the crystallographic 'a' axis, as shown in Figure 3. On the other hand, the hydrogen atom, H(1), in complex **2** forms intra dimer hydrogen bond with the symmetry related (^{b} = 1-x,2-y,2-z) phenoxo oxygen atom, O(1)^{b}, as shown in Figure 2. The details of hydrogen bonding interactions are gathered in Table 3.

*3.2.2 Complex [Cu(L)($\mu_{1,5}$-dca)]$_n$ (**3**)*

Complex **3** crystallizes in the monoclinic space group $P2_1/n$. The X-ray crystal structure determination reveals that the copper(II) centres are bridged singly by end to end dicyanamide with the formation of a zigzag chain. Perspective view of complex **3** with selective atom-numbering scheme is shown in Figure 4 and important bond lengths and bond angles are listed in Table 2. The asymmetric unit consists of a copper(II) centre, one deprotonated Schiff base ligand, (L^-), and a dca anion. Each copper(II) centre is coordinated equatorially by one imine nitrogen atom, N(2), one amine nitrogen atom, N(1) and one oxygen atom, O(1), of the tridentate deprotonated Schiff base, $(L)^-$, a nitrogen atom, N(3), of the EE bridged dca ligand. The apical position is occupied by one nitrogen atom N(5)^{c} (^{c} = -1+x,y,z) of the another EE bridged dicyanamide from a crystallographically related unit to complete elongated square-pyramidal (4 + 1) geometry for each copper(II) centre. The Addison parameter (τ) [82] is 0.29, and this confirms the slightly distorted square pyramidal geometry. In the equatorial plane, the Cu-N_{imine} distance [1.938(6) Å] is shorter than the Cu-N_{amine} [2.066(7) Å] distance, as was also observed in complexes **1** and **2**. The deviations of the coordinating atoms N(1), N(2), O(1) and N(3) from the least square mean plane through them are -0.161(7), 0.168(6) -0.158(5) and 0.151(6) Å respectively. As usual for a square pyramid structure, the copper(II) is slightly pulled out of this mean square plane towards the apical donor atom at a distance -0.2216(9) Å. The five membered chelate ring Cu(1)-N(1)-C(2)-C(3)-N(2), assumes envelope conformation with puckering

parameters q(2) = 0.434(8) Å and ϕ(2) = 72.0(8)° [83-85]. The shortest Cu···Cu distance in the chain is 7.778(1) Å.

3.3 DFT study on supramolecular assembly

We have focused the theoretical study to analyse the noncovalent interactions that play an important role in the crystal packing of **1-3** and their energetic features. Firstly, it is worthy to mention the totally different solid state structure of **1** and **2**, in spite of similar pseudohalides are used in their syntheses. This is due to the formation of intramolecular N-H···O interactions in **2** that are not formed in **1** as a consequence of the incorporation of a water molecule from the solvent in the crystal packing of **1** that interacts with the O atoms of the ligand and impede the formation of the intramolecular hydrogen bonds. This fact facilitates the formation of infinite hydrogen bonded chains in the solid state of in **1** (Figure 3) where the monomers are connected via two self-complementary N-H···N bonds. This is obviously not possible in **2**, thus generating a totally different packing.

We have first computed the Molecular Electrostatic Potential (MEP) surface of **1** and **2** in order to know those regions where the most positive and negative MEP values are located (Figure 5). It can be clearly observed that in both complexes the terminal atom of the pseudohalide ligand exhibits the most negative potential (-52 kcal mol^{-1}) followed by the oxygen atom of the organic ligand. The most significant difference between both MEP surfaces is that a strongly positive surface is found on the accessible N-H group (+41 kcal mol^{-1}) in **1**. In contrast this group is pointing to the oxygen atom of the organic ligand in **2** and the potential MEP value in that region is much smaller. Therefore, the MEP surface results indicate that **1** has a strong preference for the interaction between the pseudohalide and the N-H, as it is observed in the solid state. The MEP surfaces also

show that the electrostatic potential over the aromatic rings is negative (~-16 kcal/mol) and positive in the aliphatic hydrogen atoms (+25 kcal mol^{-1}), therefore the formation of C-H···π interactions is highly favoured.

In good agreement with the MEP surface results, the analysis of the crystal packing of **1** reveals the formation of supramolecular assemblies in the solid state that are dominated by hydrogen bonding and C-H···π interactions. They are shown in Figure 6 along with the computed interaction energies. As expected, the formation energy of the hydrogen bonded dimer (ΔE_1 = -20.7 kcal mol^{-1}; Figure 6A) is large and negative, in agreement to the MEP analysis. However, the dimer that is dominated by C-H···π interactions (Figure 6B) presents more favorable interaction energy (ΔE_2 = -29.1 kcal mol^{-1}; Figure 6A) due to the formation of six short C-H···π contacts upon complexation with are favoured electrostatically (MEP surface in Figure 5). This is likely to the anionic nature of the arene (naphtholate) and the enhanced acidity of the aliphatic hydrogen atoms due to the nitrogen coordination to the transition metal. To corroborate this, we have computed an additional model where the copper and azide co-ligands have been eliminated and the oxygen atom protonated. As a result, the interaction energy is reduced to ΔE_3 = -17.2 kcal mol^{-1} (Figure 6C), confirming the strong influence of the metal coordination on the C-H···π interaction. We have used the Bader's theory of "atoms in molecules" (AIM), which provides an unambiguous definition of chemical bonding, to further describe the C-H···π interactions observed in complex **1**. The AIM theory has been successfully used to characterize and understand a great variety of interactions. In Figure 6D we show the AIM analysis of the C-H···π model complex of complex **1** and it can be observed that each C-H···π interaction is characterized by the presence of one bond critical point (red sphere) that connects the hydrogen atom to one carbon atom of the ring. As a consequence, two ring critical points (yellow spheres) are also generated upon complexation due to the formation of the supramolecular rings.

The formation of the intramolecular N-H···O hydrogen bonds in **2** is due to the absence of the water solvent molecule affects the crystal packing. In Figure 7A we show an interesting assembly found in the solid state structure of **2** where a combination of C-H···O hydrogen bonds, C-H···π and π···π interactions are established. In fact, this assembly is infinitely repeated in the solid state generating an infinite 1D ladder where the two different π···π stacking interactions participate. One of them is assisted by a C-H···π interaction and the other one is assisted by two symmetrically related hydrogen bonding interactions. We have evaluated energetically both binding modes using several theoretical models. The interaction energy of the C-H···π assisted one (Figure 7B) is large and negative (ΔE_4 = -23.2 kcal mol^{-1}) likely due to the influence of the metal coordination that enhances the C-H···π interaction. In fact, we have computed an additional model (Figure 7B) where the metal ion has been eliminated and the oxygen atom protonated and the interaction energy is reduced to ΔE_4 = -15.7 kcal mol^{-1}, confirming this explanation. The hydrogen bonding assisted π···π complex (Figure 7D) exhibits a very large binding energy ΔE_6 = -43.0 kcal mol^{-1} due to the presence of two bifurcated hydrogen bonding interactions involving the O atom of the pseudohalide ligand, which is where the most negative part of the MEP surface is located. In order to estimate the contribution of the π···π stacking interaction, we have computed an additional model where the metal and pseudohalide ligands are not present. As a results the interaction energy is dramatically reduced to ΔE_7 = -9.0 kcal mol^{-1}, that corresponds to the π···π stacking contribution.

As described above, **3** is a polymeric chain where the asymmetric units are connected by the ditopic dicyanamide anion. Actually, the solid state architecture of **3** is dominated by the coordination bonds between the end to end dca ligands and the metal centres. This likely explains the fact that the strong hydrogen bond acceptor group (N-H) does not participate in H-bonding interactions in the crystal packing. The infinite chains are connected to each other via two types of π···π stacking

interactions (Figure 8A) resembling an infinite zipper. We have denoted both stacking interactions as $(\pi\cdots\pi)_1$ and $(\pi\cdots\pi)_2$ and a close examination of both binding modes reveals that $(\pi\cdots\pi)_2$ is a conventional parallel displaced π···π stacking interaction and also discloses that additional interactions are established in $(\pi\cdots\pi)_1$. Therefore, we have examined latter binding mode theoretically to characterize the different interactions. The binding energy (Figure 8B) computed for a model of the $(\pi\cdots\pi)_1$ stacking interaction is very large (ΔE_8 = -32.7 kcal mol^{-1}) due to the participation of additional C-H···π and N-H···π interactions and the influence of the metal coordination. In this theoretical model we have used HCN/CN^- instead of the dicyanamide in order to simplify the polymeric chain and keep the charge of the model neutral. We have also computed the influence of the metal coordination on the interaction energy and, similarly to previous observations, it is very important since the interaction energy is reduced from ΔE_8 = -32.7 kcal mol^{-1} to ΔE_9 = -15.6 kcal mol^{-1} (Figure 8C) if the metal centres are eliminated. Furthermore, we have used the Bader's theory of "atoms in molecules" (AIM), to further demonstrate the existence of the electrostatically favored N-H···π interaction observed in **3**. In Figure 8D we show the AIM analysis of the $(\pi\cdots\pi)_1$ model complex and it can be observed the presence of two N-H···π and two C-H···π interactions. Each one is characterized by the presence of one bond critical point (red sphere) that connects the hydrogen atom to one carbon atom of the ring. The distribution of critical points also reveals the presence of three bond paths with the corresponding critical bond critical points connecting three aromatic carbon atoms, which characterize the π···π interaction. As a consequence, several ring and cage critical points (yellow and cage spheres) are also generated upon complexation due to the formation of the supramolecular rings and cages.

3.4 Magnetic properties and epr spectroscopy

The variable temperature magnetic properties (in the range of 2 - 300 K) of three complexes in the form of $\chi_M T$ vs T (χ_M vs T inset) plots are illustrated in Figures 9-11 respectively ($\chi_M T$ is the molar susceptibility for two copper(II)). Both complexes **1** and **3** show similar $\chi_M T$ vs T plots. At room temperature (300 K), the $\chi_M T$ values are of 0.802 cm^3 K mol^{-1} (for **1**) and 1.777 cm^3 K mol^{-1} (for **3**). The $\chi_M T$ value remains practically constant up to 50 K for both complexes. As the temperature continues to decrease, it begins to decrease due to antiferromagnetic exchange coupling between copper(II) centres. On the other hand, complex **2** exhibited temperature independent $\chi_M T$ value between 25-300 K. Below 25 K it shows a upturn in the $\chi_M T$ value due to ferromagnetic exchange coupling between copper(II) centres.

Since **1** and **2** are present as isolated copper(II) dimers with double asymmetric end on pseudohalide bridges (azide in **1**; cyanate in **2**), we used a simple Bleaney-Bowers dimer model for two $S = {}^1/_2$ ions to fit the magnetic data [86]. This model reproduces very satisfactorily magnetic properties of both complexes in the whole temperature range. Simulation of both $\chi_M T$ vs T and χ_M vs T plots were performed using $\hat{H} = -2JS_1 \cdot S_2 + \mu_B gSH$ (the standard Heisenberg-Dirac-van Vleck Hamiltonian). A good fit for the $\chi_M T$ versus T data of complex **1** has been obtained for the parameters $g = 2.103$ and $J = -2.313$ cm^{-1}. The fit included a minor contribution from the temperature independent paramagnetism (40×10^{-6} cm^3 mol^{-1} for **1**) [87]. The magnetic property of complex **1** has been compared with other reported antiferromagnetic asymmetric double end on azide bridged copper(II) complexes with 'half salen' type Schiff base ligands (Table 4). Although both Cu–N_{azide} bond distances and Cu–N_{azide}–Cu angle have pronounced effects on the magnetic coupling through asymmetric double end on azide bridges, the main parameter determining the magnetic exchange seems to be the long

$Cu\text{-}N_{azide}$ bond distance. It explains the weak antiferromagnetic exchange observed in 1. Similar conclusion has also been drawn by other groups [31].

On the other hand, complex **2** shows a $\chi_M T$ value of 0.850 cm^3 K mol^{-1} at room temperature, which increases to 0.976 cm^3 K mol^{-1} at 2 K. Complex **2**, which shows ferromagnetic exchange interactions, gave a best fit for g = 2.141 and J = 0.513 cm^{-1} (Figure 10). The only previously reported double $\mu_{1,1}$ cyanate bridged dinuclear copper(II) complex with half salen as blocking ligand exhibits antiferromagnetic exchange coupling between copper(II) centres with J = -0.54 cm^{-1} and g = 2.072 [24]. With the addition of a methyl group at the amine nitrogen atom of the Schiff base of the reported complex [24], the $Cu\text{–}N_{cyanate}\text{–}C_{cyanate}$ angle has increased from 153° to 162°. The cyanate ligand in **2** is pitched at a very different angle to that of azide ligand in **1** ($Cu\text{–}N_{azide}\text{–}N_{azide}$ = 134°). Hydrogen bonds to phenoxo oxygen atoms are causing this angle to increase in case of cyanate which may be the cause for the observed change in sign of J. A satisfactory fit required inclusion of TIP of -210 × 10^{-6} cm^3 mol^{-1} [87].

In case of complex **3**, four independent spin-half copper(II) centres with equivalent exchange coupling constants (J_{12} = J_{23} = J_{34}) have been used to model the data since complex **3** represents a chain of end to end dca bridged copper(II) centres. A good fit for the $\chi_M T$ vs T data has been obtained for the parameters g = 2.192 and J = -0.344 cm^{-1} having a TIP value of -400 × 10^{-6} cm^3 mol^{-1}. Literature shows that similar end to end dca bridged polynuclear copper(II) complexes have similar values [24,88].

The fluid solution EPR spectra recorded at 293 K are typical of copper(II) species (Figures 12-14). Each compound gave near identical spectrum consistent with mononuclear copper species that form when dimeric **1** and **2**, and polymeric **3** are dissolved in solution. This outcome was independent

of the choice of solvent, which ranged from potentially ligating DMF and MeCN, to non-coordinating CH_2Cl_2. The spectra were simulated giving spin-Hamiltonian parameters: g = 2.096, A^{Cu} = 77 × 10^{-4} cm^{-1} (**1**); g = 2.103, A^{Cu} = 75 × 10^{-4} cm^{-1} (**2**); g = 2.102, A^{Cu} = 77.5 × 10^{-4} cm^{-1} (**3**). The nearly identical parameters underscore the similarity of the copper(II) coordination sphere. Moreover, the g-values match nicely with those obtained from magnetic susceptibility.

3.5 DFT study on magnetic properties

We have analysed the magnetic coupling interaction theoretically in the dinuclear **1** and **2** by computing the Mulliken spin density distribution. According to the molecular orbital theory, spin delocalization is the result of electron transfer from the magnetic centres to the ligand atoms. For this theoretical study we have used the crystal structure geometries. The calculation of the individual pairwise exchange constants have been carried out by means of spin-unrestricted DFT calculations using the B3LYP method and employing the 6-31+G* basis set. Since each complex (**1** or **2**) features one unpaired electron on each copper ion, they constitute a set of magnetically coupled spin centres [89-90] whose interaction is quantified by the Heisenberg exchange coupling constant, J [91-94]. For the modelling of the magnetic properties of the present systems, the broken symmetry (BS) approach was used [95-97]. The theoretical J-value calculation has been performed computing the difference between the energy values of the high-spin (HS) state and the broken symmetry state. Using this methodology, the resulting theoretical J-values obtained for **1** and **2** are -2.50 cm^{-1} and 0.75 cm^{-1}, respectively, which are in excellent agreement with the experimental values (-2.31 and 0.51 cm^{-1} for **1** and **2**, respectively) and confirms the weak antiferromagnetic coupling between both metal centres in **1** and, conversely, ferromagnetic coupling in **2**. The Mulliken spin population analyses (Table 5) for the HS configuration of **1** and **2** indicate that a significant spin (ca. 0.86 e) is delocalized through the

ligands, and the rest (1.14 e) is carried by the copper atoms. For the low spin configuration of **1**, the spin densities of +0.58 on one copper(II) and -0.58 on the other confirms that they are the magnetic centres, and the spin densities on the ligand atoms have the same signs as that of the copper(II) atoms to which they are bonded (Table 5). The spin density values at the bridging nitrogens (belonging to the pseudohalides) are small; thus weak magnetic coupling is mediated through the bridging ligands communicating the magnetic orbitals, in agreement with the small *J*-values.

In square-pyramidal copper(II) complexes, the $d_{x^2-y^2}$ orbital contains the unpaired electron; consequently, these orbitals along with the local orbitals of the bridging ligands are involved in the super exchange pathway, which is confirmed by the SOMOs shown in Figure 15 for complexes **1** and **2**. The spin density plots are also shown in Figure 15 for the low spin state (one broken symmetry solution) of complex **1** and high spin state of **2**. The spin density distributions show a delocalization mechanism in which the copper atoms carry ~57% of net spin and the remaining part is delocalized through the coordinating atoms.

3.6 IR and electronic spectra

Strong and sharp bands around 1620 cm^{-1} were routinely noticed due to imine (C=N) groups of Schiff bases in the IR spectra of all three complexes [79]. One moderately strong band in the region of 3300-3400 cm^{-1} in the IR spectrum of each complex is observed due to N–H stretching vibrations [79]. An intense absorption band at 2033 cm^{-1} in the IR spectrum of complex **1** indicates the presence of azide [24]. Presence of the nitrogen bonded cyanate in complex **2** is confirmed by the strong band at 2215 cm^{-1} [24]. Presence of dicyanamide in complex **3** is indicated by the bands at 2178, 2232 and 2287 cm^{-1} [98].

The electronic spectrum of each complex in acetonitrile displays a single broad absorption band around 590 nm. Copper(II), in square pyramidal environment, usually have three transitions in between of $^2A_{1g} \leftarrow {}^2B_{1g}$, $^2B_{2g} \leftarrow {}^2B_{1g}$, and $^2E_g \leftarrow {}^2B_{1g}$ states. The broad absorption band is due to two overlapping bands corresponding to $^2B_{2g} \leftarrow {}^2B_{1g}$, and $^2E_g \leftarrow {}^2B_{1g}$ states [99]. The UV absorption bands around 310 nm may be assigned to intra ligand $\pi^* \leftarrow n$ transitions of azomethine (C=N) function of Schiff base [100-101]. The band around 390 nm may be attributed to LMCT transition from the N donor centres of Schiff base to copper(II).

3.7 ESI mass spectroscopy

The electron spray ionization mass spectrum is useful to know the nature of complexes in solution. The ESI-MS positive spectra of all three complexes have been recorded in the acetonitrile solution. The experimentally observed peaks along with their isotopic distribution patterns correspond very well to that of their corresponding simulated spectral patterns. In the mass spectrum of complex **1**, the peak at *m/z* = 665.12 indicates the presence of $[\{Cu_2(L)_2(\mu_{1,1}\text{-}N_3)_2\}H]^+$. The peaks at 666.12, 667.12, 668.12 and 669.12 are due to isotopic distribution (Figure 16). Complex **2** exhibits quite similar mass spectrum giving peak at *m/z* = 665.09. Complex **3** shows peak at *m/z* = 645.96 (along with peaks at 647.97, 649.01, 650.01 due to isotopic distribution) which corresponds to $[Cu_2L_2(dca)]^+$. In this mass spectrum (Figure 17), peak at *m/z* = 289.99 (along with peaks at 291.02, 292.01 and 293.01) corresponds to the presence of $[CuL]^+$ formed by the removal of bridging dicyanamides.

3.8 X-ray powder diffraction pattern

The experimental PXRD patterns of the bulk products are in good agreement with the simulated XRD patterns from single-crystal X-ray diffraction, indicating consistency of the bulk sample. The simulated patterns of the complexes are calculated from the single crystal structural data (cifs) using the CCDC Mercury software. Figures 18-20 show the experimental and simulated XRD patterns for complexes **1-3**.

3.9 Hirshfeld surface analysis

The Hirshfeld surfaces of all three complexes, mapped over d_{norm} (range of -0.1 to 1.5 Å), shape index and curvedness, are illustrated in Figure 21. The surfaces are shown as transparent to allow visualization of the molecular moiety around which they are calculated. The dominant interaction between O···H atoms can be seen in the Hirshfeld surfaces as red spots on the d_{norm} surface in Figure 21. Other visible spots in the Hirshfeld surfaces correspond to H···H contacts. The small extent of area and light colour on the surface indicates weaker and longer contact other than hydrogen bonds. The intermolecular interactions appear as distinct spikes in the 2D fingerprint plot (Figure 22). Complementary regions are visible in the fingerprint plots where one molecule acts as donor ($d_e > d_i$) and the other as an acceptor ($d_e < d_i$). The fingerprint plots can be decomposed to highlight particular atoms pair close contacts [102]. This decomposition enables separation of contributions from different interaction types, which overlap in the full fingerprint. The proportions of N···H/H···N interactions comprise 17.4% of the total Hirshfeld surfaces for each molecule of **1**. This N···H/H···N interaction appears as two distinct spikes in the 2D fingerprint plots (Figure 22). The lower spike corresponding to the acceptor spike represents the N···H interactions (d_i = 1.3, d_e = 0.9 Å) and the

upper spike being a donor spike represents the H···N interactions (d_e = 1.3, d_i = 0.9 Å) in the fingerprint plots. In case of **2** proportions of O···H/H···O interactions comprise 19.9% of the total Hirshfeld surfaces for each molecule. This O···H/H···O interaction also appears as two distinct spikes in the 2D fingerprint plots (Figure 22). The lower spike corresponding to the acceptor spike represents the O···H interactions (d_i = 1.25, d_e = 0.95 Å) and the upper spike being a donor spike represents the H···O interactions (d_e = 1.25, d_i = 0.95 Å) in the fingerprint plots. The proportions of N···H/H···N interactions comprise 18% of the total Hirshfeld surfaces for each molecule of **3**. The lower spike corresponding to the acceptor spike represents the N···H interactions (d_i = 1.5, d_e = 1.15 Å) and the upper spike being a donor spike represents the H···N interactions (d_e = 1.15, d_i = 1.5 Å) in the fingerprint plots.

4. Concluding Remarks

In this paper we report synthesis and characterization of two dinuclear $[Cu_2(L)_2(\mu_{1,1}\text{-}N_3)_2]\cdot H_2O$ (**1**) and $[Cu_2(L)_2(\mu_{1,1}\text{-}NCO)_2]$ (**2**) and one polynuclear $[Cu(L)(\mu_{1,5}\text{-}dca)]_n$ (**3**) complexes of copper(II) by using a tridentate N_2O donor Schiff base along with azide, cyanate or dicyanamide as co-ligands. Single crystal X-ray diffraction analysis reveals that coordination geometry around copper(II) centres in all complexes are elongated (4+1) square pyramidal. The structural change from dimer to polymer has been facilitated by the replacing of azide/cyanate with dicyanamide. Variable temperature magnetic susceptibility data over the range 2-300 K shows antiferromagnetic exchange coupling between copper(II) centres in **1** and **3** whereas ferromagnetic exchange coupling in **2**. The relevant noncovalent interactions observed in the solid state have been rationalized using DFT calculations, including MEP and AIM analyses and we have assigned discrete interaction energies to them. The C-H···π and π···π interactions are crucial in the crystal packing of the complexes, even in

the presence of strong hydrogen bonding interactions. They are also responsible of the formation of a supramolecular zipper in the solid state structure of **3**.

Acknowledgements

A.B. thanks the UGC, India, for awarding a Senior Research Fellowship. Crystallographic data were collected at the DST-FIST, India funded Single Crystal Diffractometer Facility at the Department of Chemistry, Jadavpur University. S.S. thanks the RSC for a J. W. T. Jones Travelling Fellowship.

Appendix A. Supplementary data

CCDC 1053629-1053631 contain the supplementary crystallographic data for complexes **1** – **3**. These data can be obtained free of charge via http://www.ccdc.cam.ac.uk/conts/retrieving.html, or from the Cambridge Crystallographic Data Centre, 12 Union Road, Cambridge CB2 1EZ, UK; fax: (+44) 1223-336-033; or e-mail: deposit@ccdc.cam.ac.uk.

References

[1] C. Biswas, S. Chattopadhyay, M. G. B. Drew, A. Ghosh, Polyhedron 26 (2007) 4411-4418.

[2] H. Y. Zang, Y. Q. Lan, G. S. Yang, X. L. Wang, K. Z. Shao, G. J. Xu, Z. M. Su, CrystEngComm. 12 (2010) 434-445.

[3] M. das, S. Chatterjee, S. Chattopadhyay, Polyhedron 68 (2014) 205-211.

[4] Z. N. Chen, H. X. Zhang, K. B. Yu, K. C. Zheng, H. Cai, B. S. Kang, J. Chem. Soc., Dalton Trans. (1998) 1133-1136.

[5] A. Bacchi, M. Carcelli, T. Chiodo, P. Pelagatti, CrystEngComm. 12 (2010) 4226-4230.

[6] M. Das, S. Chattopadhyay, Polyhedron 50 (2013) 443-451.

[7] R. Biswas, Y. Ida, M. L. Baker, S. Biswas, P. Kar, H. Nojiri, T. Ishida, A. Ghosh, Chem. Eur. J. 19 (2013) 3943-3953.

[8] L. -Z. Chen, D. -D. Huang, J. -Z. Ge, F. -M. Wang, Inorg. Chim. Acta 406 (2013) 95-99.

[9] Y. Wang, Y. -X. Che, J. -M. Zheng, Inorg. Chem. Commun. 21 (2012) 69-71.

[10] E. I. Solomon, U. M. Sundaram, T. E. Machonkin, Chem. Rev. 96 (1996) 2563-2606.

[11] C. Biswas, M. G. B. Drew, E. Ruiz, M. Estrader, C. Diaz, A. Ghosh, Dalton Trans. 39 (2010) 7474-7484.

[12] C. Biswas, M. G. B. Drew, A. Figuerola, S. Gómez-Coca, E. Ruiz, V. Tangoulis, A. Ghosh, Inorg. Chim. Acta 363 (2010) 846-854.

[13] A. Biswas, L. K. Das, M. G. B. Drew, C. Diaz, A. Ghosh, Inorg. Chem. 51 (2012) 10111–10121.

[14] C. Biswas, M. G. B. Drew, S. Asthana, C. Desplanches, A. Ghosh, J. Mol. Struc. 965 (2010) 39-44.

[15] P. K. Bhowmik, S. Chattopadhyay, Inorg. Chem. Commun. 22 (2012) 14-17.

[16] M. Das, B. N. Ghosh, A. Valkonen, K. Rissanen, S. Chattopadhyay, Polyhedron 60 (2013) 68-77.

[17] P. K. Bhaumik, K. Harms, S. Chattopadhyay, Inorg. Chim. Acta 405 (2013) 400-409.

[18] S. Mukherjee, P. S. Mujherjee, Acc. Chem. Res. 46 (2013) 2556-2566.

[19] A. Bhattacharyya, B. N. Ghosh, K. Rissanen, R. Jiménez-Aparicio, S. Chattopadhyay, Dalton Trans. 44 (2015) 493-497.

[20] P. Talukder, A. Datta, S. Mitra, G. Rosair, M. S. E. Fallah, J. Ribas, Dalton Trans. (2004) 4161-4167.

[21] S. Paul, R. Clerac, N. G. R. Hearns, D. Ray, Cryst. Growth Des. 9 (2009) 4032-4040.

[22] P. K. Bhaumik, K. Harms, S. Chattopadhyay, Inorg. Chim. Acta 405 (2013) 400–409.

[23] C. Adhikary, S. Koner, Coord. Chem. Rev. 254 (2010) 2933-2958 and references there in.

[24] P. Bhowmik, A. Bhattacharyya, K. Harms, S. Sproules, S. Chattopadhyay, Polyhedron 85 (2015) 221-231.

[25] M. S. Ray, A. Ghosh, S. Chaudhuri, M. G. B. Drew, J. Ribas, Eur. J. Inorg. Chem. (2004) 3110-3117.

[26] S. Koner, S. Saha, T. Mallah, K.-I. Okamoto, Inorg. Chem. 43 (2004) 840-842.

[27] M. Zbiri, S. Saha, C. Adhikary, S. Chaudhuri, C. Daul, S. Koner, Inorg. Chim. Acta 359 (2006) 1193-1199.

[28] C. Adhikary, R. Sen, G. Bocelli, A. Cantoni, S. Chaudhuri, S. Koner, J. Coord. Chem. 62 (2009) 3573-3582.

[29] S. Mondal, P. Chakraborty, N. Aliaga-Alcalde, S. Mohanta, Polyhedron 63 (2013) 96-102.

[30] S. Jana, B. K. Shaw, P. Bhowmik, K. Harms, M. G. B. Drew, S. Chattopadhyay, S. K. Saha, Inorg. Chem. 53 (2014) 8723-8734.

[31] S. Triki, C. J. Gomez-Garcıa, E. Ruiz, J. Sala-Pala, Inorg. Chem. 44 (2005) 5501-5508.

[32] S. Sen, S. Mitra, D. L. Hughes, G. Rosair, C. Desplanches, Inorg. Chim. Acta 360 (2007) 4085-4092.

[33] S. Banerjee, S. Sen, S. Basak, S. Mitra, D. L. Hughes, C. Desplanches, Inorg. Chim. Acta 361 (2008) 2707-2714.

[34] G. R. Desiraju, Acc. Chem. Res. 35 (2002) 565-573.

[35] G. R. Desiraju, Nature 412 (2001) 397-400.

[36] H. M. Lee, S. B. Suh, J. Y. Lee, P. Tarakeshwar, K. S. Kim, J. Chem. Phys. 112 (2000) 9759-9772.

[37] B. H. Hong, J. Y. Lee, C.-W. Lee, J. C. Kim, S. C. Bae, K. S. Kim, J. Am. Chem. Soc. 123 (2001) 10748-10749.

[38] T. Steiner, Angew. Chem. Int. Ed. 41 (2002) 48-76.

[39] C. A. Hunter, J. K. M. Sanders, J. Am. Chem. Soc. 112 (1990) 5525-5534.

[40] S. K. Burley, G. A. Petsko, Science 229 (1985) 23-28.

[41] K. S. Kim, P. Tarakeshwar, J. Y. Lee, Chem. Rev. 100 (2000) 4145–4185.

[42] J. C. Ma, D. A. Dougherty, Chem. Rev. 97 (1997) 1303–1324.

[43] K. S. Kim, J. Y. Lee, S. J. Lee, T.-K. Ha, D. H. Kim, J. Am. Chem. Soc. 116 (1994) 7399-7400.

[44] D. Quinonero, C. Garau, C. Rotger, A. Frontera, P. Ballester, A. Costa, P. M. Deya, Angew. Chem. Int. Ed. 41 (2002) 3389-3392.

[45] M. Egli, S. Sarkhel, Acc. Chem. Res. 40 (2007) 197-205.

[46] T. J. Mooibroek, P. Gamez, J. Reedijk, CrystEngComm. 10 (2008) 1501-1515.

[47] J. Ran, P. Hobza, J. Chem. Theory Comput. 5 (2009) 1180-1185.

[48] M. Barcelo-Oliver, C. Estarellas, A. Garcıa-Raso, A. Terron, A. Frontera, D. Quinonero, E. Molins, P. M. Deya, CrystEngComm. 12 (2010) 362-365.

[49] M. Nishio, M. Hirota, Y. Umezawa, *The C-H···π Interaction: Evidence, Nature, Consequences*, Wiley-VCH, New York, 1998.

[50] M. Nishio, CrystEngComm 6 (2004) 130-156.

[51] G. R. Hanson, K. E. Gates, C. J. Noble, M. Griffin, A. Mitchell, S. Benson, J. Inorg. Biochem. 98 (2004) 903-916.

[52] G. M. Sheldrick, Acta Crystallogr. Sect. A 64 (2008) 112-122.

[53] G. M. Sheldrick, *SHELXS-97 and SHELXL-97, Program for Structure Solution*, University of Göttingen, Germany, 1997.

[54] G. M. Sheldrick, *SADABS, Software for Empirical Absorption Correction*, University of Göttingen, Institute fur Anorganische Chemieder Universitat, Gottingen, Germany, 1999-2003.

[55] R. Ahlrichs, M. Bär, M. Häser, H. Horn, C. Kölmel, Chem. Phys. Lett. 162 (1989) 165-169.

[56] A. Bauzá, A. Terrón, M. Barceló-Oliver, A. García-Raso, A. Frontera, Inorg. Chim. Acta. 452 (2016) 244-250.

[57] D. Sadhukhan, M. Maiti, G. Pilet, A. Bauzá, A. Frontera, S. Mitra, Eur. J. Inorg. Chem. 11 (2015) 1958-1972.

[58] M. Mirzaei, H. Eshtiagh-Hosseini, Z. Bolouri, Z. Rahmati, A. Esmaeilzadeh, A. Hassanpoor, A. Bauza, P. Ballester, M. Barceló-Oliver, J. T Mague, B. Notash, A. Frontera, Cryst. Growth Des. 15 (2015) 1351-1361.

[59] P. Chakraborty, S. Purkait, S. Mondal, A. Bauzá, A. Frontera, C. Massera, D. Das, CrystEngComm 17 (2015) 4680-4690.

[60] S. F. Boys, F. Bernardi, Mol. Phys. 19 (1970) 553-566.

[61] R. F. W. Bader, Chem. Rev. 91 (1991) 893-928.

[62] *AIMAll* (Version 13.05.06) A. Todd, T. K. Keith, Gristmill Software, Overland Park KS, USA, 2013.

[63] A. D. Becke, Phys. Rev. A 38 (1988) 3098-3100.

[64] C. T. Lee, W. T. Yang, R. G. Parr, Phys. Rev. B 37 (1988) 785-789.

[65] A. D. Becke, J. Chem. Phys. 98 (1993) 5648-5653.

[66] M. J. Frisch, G. W. Trucks, H. B. Schlegel, G. E. Scuseria, M. A. Robb, J. R. Cheeseman, G. Scalmani, V. Barone, B. Mennucci, G. A. Petersson, H. Nakatsuji, M. Caricato, X. Li, H. P. Hratchian, A. F. Izmaylov, J. Bloino, G. Zheng, J. L. Sonnenberg, M. Hada, M. Ehara, K. Toyota, R. Fukuda, J. Hasegawa, M. Ishida, T. Nakajima, Y. Honda, O. Kitao, H. Nakai, T. Vreven, J. A. Montgomery, Jr., J. E. Peralta, F. Ogliaro, M. Bearpark, J. J. Heyd, E. Brothers, K. N. Kudin, V. N. Staroverov, R. Kobayashi, J. Normand, K. Raghavachari, A. Rendell, J. C. Burant, S. S. Iyengar, J. Tomasi, M. Cossi, N. Rega, J. M. Millam, M. Klene, J. E. Knox, J. B. Cross, V. Bakken, C. Adamo, J. Jaramillo, R. Gomperts, R. E. Stratmann, O. Yazyev, A. J. Austin, R. Cammi, C. Pomelli, J. W. Ochterski, R. L. Martin, K. Morokuma,

V. G. Zakrzewski, G. A. Voth, P. Salvador, J. J. Dannenberg, S. Dapprich, A. D. Daniels, Ö. Farkas, J. B. Foresman, J. V. Ortiz, J. Cioslowski, D. J. Fox, *Gaussian 09*, Revision B.01, Gaussian, Inc., Wallingford CT, 2009.

[67] E. Ruiz, J. Cano, S. Alvarez, P. Alemany, J. Comput. Chem. 20 (1999) 1391-1400.

[68] E. Ruiz, S. Alvarez, A. Rodríguez-Fortea, P. Alemany, Y. Pouillon, C. Massobrio, *Magnetism: Molecules to Materials* (Eds.: J. S. Miller, M. Drillon), Wiley-VCH, Weinheim, Germany, 2001.

[69] E. Ruiz, A. R. -Fortea, J. Cano, S. Alvarez, P. Alemany, J. Comput. Chem. 24 (2003) 982-989.

[70] E. Ruiz, S. Alvarez, J. Cano, V. Polo, J. Chem. Phys. 123 (2005) 164110-164117.

[71] M. A. Spackman, D. Jayatilaka, CrystEngComm 11 (2009) 19-32.

[72] F. L. Hirshfeld, Theor. Chim. Acta 44 (1977) 129-138.

[73] H. F. Clausen, M. S. Chevallier, M. A. Spackman, B. B. Iversen, New J. Chem. 34 (2010) 193-199.

[74] A. L. Rohl, M. Moret, W. Kaminsky, K. Claborn, J. J. McKinnon, B. Kahr, Cryst. Growth Des. 8 (2008) 4517-4525.

[75] A. Parkin, G. Barr, W. Dong, C. J. Gilmore, D. Jayatilaka, J. J. McKinnon, M. A. Spackman, C. C. Wilson, CrystEngComm 9 (2007) 648-652.

[76] M. A. Spackman, J. J. McKinnon, CrystEngComm 4 (2002) 378-392.

[77] S. K. Wolff, D. J. Grimwood, J. J. McKinnon, D. Jayatilaka, M. A. Spackman, Crystal Explorer 2.0; University of Western Australia: Perth, Australia, 2007; http://hirshfeldsurfacenet.blogspot.com

[78] J. J. McKinnon, M. A. Spackman, A. S. Mitchell, Acta Crystallogr. Sect. B 60 (2004) 627-668.

[79] M. Das, S. Chattopadhyay, Transition. Met. Chem. 38 (2013) 191-197.

[80] P. K. Bhaumik, K. Harms, S. Chattopadhyay, Polyhedron 67 (2014) 181-190.

[81] P. K. Bhaumik, K. Harms, S. Chattopadhyay, Polyhedron 62 (2013) 179-187.

[82] A. W. Addison, T. N. Rao, J. Reedjik, J. van Rinj, C. G. Verscholar, J. Chem. Soc., Dalton Trans. (1984) 1349-1356.

[83] D. Cremer, J. A. Pople, J. Am. Chem. Soc. 97 (1975) 1354-1358.

[84] D. Cremer, Acta Crystallogr. Sect. B 40 (1984) 498-500.

[85] J. C. A. Boeyens, J. Cryst. Mol. Struct. 8 (1978) 317-320.

[86] B. Bleaney, K. D. Bowers, Proc. R. Soc. London Ser. A214 (1952) 451-465.

[87] O. Kahn, *Molecular Magnetism*, VCH, New York, 1993.

[88] R. Karmakar, C. R. Choudhury, D. L. Hughes, G. P. A. Yap, M. S. El Fallah, C. Desplanches, J. -P. Sutter, S. Mitra, Inorg. Chim. Acta 359 (2006) 1184-1192.

[89] A. Bencini, D. Gatteschi, *Electron Paramagnetic Resonance of Exchange Coupled Systems*, Springer, Berlin, 1990.

[90] O. Kahn, *Molecular Magnetism*, VCH, New York, 1993.

[91] W. Z. Heisenberg, Physik 38 (1926) 411-426.

[92] W. Z. Heisenberg, Physik 49 (1928) 619-636.

[93] P. A. M. Dirac, Proc. R. Soc. London Ser. A123 (1929) 714-733.

[94] J. H. Van Vleck, *The Theory of Electronic and Magnetic Susceptibilies*, Oxford University, London, 1932.

[95] L. Noodleman, J. Chem. Phys. 74 (1981) 5737-5743.

[96] L. Noodleman, D. A. Case, Adv. Inorg. Chem. 38 (1992) 423-470.

[97] L. Noodleman, E. R. Davidson, Chem. Phys. 109 (1986) 131-143.

[98] A. Bhattacharyya, S. Sen, K. Harms, S. Chattopadhyay, Polyhedron 88 (2015) 156-163.

[99] D. Matoga, J. Szklarzewicz, R. Grybos, K. Kurpiewska, W. Nitek, Inorg. Chem. 50 (2011) 3501-3510.

[100] U. Singh, M. M. Dar, S. Anayutullah, H. Alam, N. Manzoor, S. Ahmed Al-Thabaiti, A. A. Hashmi, J. Coord. Chem. 68 (2015) 2096-2106.

[101] P. R. Reddy, A. Shilpa, N. Raju, P. Raghavaiah, J. Inorg. Biochem. 105 (2011) 1603-1612.

[102] M. A. Spackman, P. G. Byrom, Chem. Phys. Lett. 267 (1997) 215-220.

Table 1: Crystal data and refinement details of complexes **1-3**.

	1	**2**	**3**
Formula	$C_{28}H_{32}Cu_2N_{10}O_3$	$C_{30}H_{30}Cu_2N_6O_4$	$C_{16}H_{15}CuN_5O$
Formula Weight	683.74	665.70	356.88
Temperature(K)	100	100	100
Crystal system	Monoclinic	Triclinic	Monoclinic
Space group	*C2/c*	*P-1*	$P2_1/n$
a(Å)	22.7268(19)	7.2270(3)	7.7783(5)
b(Å)	9.5719(7)	8.7076(4)	12.6455(9)
c(Å)	14.6305(11)	11.0944(6)	15.1497(9)
α(deg)	(90)	84.120(4)	(90)
β(deg)	112.744(9)	86.489(4)	98.037(4)
γ(deg)	(90)	89.237(4)	(90)
Z	4	1	4
d_{calc}(g cm^{-3})	1.547	1.595	1.607
μ(mm^{-1})	1.498	1.583	1.492
F(000)	1408	342	732
Total Reflections	18115	10161	20106
Unique Reflections	2314	2617	2814
Observed data [I > 2 σ (I)]	1696	1900	1643
No. of parameters	200	190	212
R(int)	0.096	0.052	0.080
R1, wR2(all data)	0.0735, 0.1525	0.0766, 0.1437	0.1284, 0.2487
R1, wR2 [I > 2 σ (I)]	0.0526, 0.1345	0.0507, 0.1291	0.0764, 0.2133

Table 2: Selected bond lengths (Å) and bond angles (°) around copper(II) for complexes **1**-**3**.

Complex	**1**	**2**	**3**
	Bond lengths		
Cu(1)-O(1)	1.908(4)	1.914(3)	1.913(5)
Cu(1)-N(1)	2.028(5)	2.036(4)	2.066(7)
Cu(1)-N(2)	1.936(4)	1.922(3)	1.938(6)
Cu(1)-N(3)	1.979(5)	1.937(4)	1.998(6)
Cu(1)-N(3)$^{\psi}$	2.442(5)	2.692(4)	-
Cu(1)-N(5)$^{\psi}$	-	-	2.337(8)
	Bond angles		
O(1)-Cu(1)-N(1)	171.49(18)	171.32(16)	174.6(2)
O(1)-Cu(1)-N(2)	90.81(18)	92.28(14)	92.2(2)
O(1)-Cu(1)-N(3)	90.79(18)	91.85(15)	92.4(3)
O(1)-Cu(1)-N(3)$^{\psi}$	94.42(17)	89.80(13)	-
O(1)-Cu(1)-N(5)$^{\psi}$	-	-	93.2(2)
N(1)-Cu(1)-N(2)	84.50(19)	84.60(14)	83.1(3)
N(1)-Cu(1)-N(3)	93.38(19)	92.38(15)	91.0(3)
N(1)-Cu(1)-N(3)$^{\psi}$	93.36(17)	82.50(15)	-
N(2)-Cu(1)-N(3)	175.41(19)	171.23(17)	157.0(3)
N(2)-Cu(1)-N(3)$^{\psi}$	99.65(16)	96.13(14)	-
N(3)-Cu(1)-N(3)$^{\psi}$	84.51(17)	91.62(16)	-
N(1)-Cu(1)-N(5)$^{\psi}$	-	-	90.2(3)
N(2)-Cu(1)-N(5)$^{\psi}$	-	-	98.7(3)
N(3)-Cu(1)-N(5)$^{\psi}$	-	-	103.5(3)

$^{\psi}$ = Symmetry transformation; $^{\psi}$ = ^{a} = -x,-y,1-z in **1**, $^{\psi}$ = ^{b} = 1-x,2-y,2-z in **2** and $^{\psi}$ = ^{c} = -1+x,y,z in **3**.

Table 3: Hydrogen bonding details of complexes **1** and **2**.

Complex	D-H···A	D-H(Å)	D···A(Å)	H···A(Å)	∠D-H···A(°)
1	N(1)-H(1)···N(5)[d]	0.7600	3.096	2.3900	155.00
2	N(1)-H(1)···O(1)[b]	0.9100	3.148	2.2900	157.00

Symmetry transformations: [d] = -x,-y,1-z; [b] = 1-x,2-y,2-z. D = donor; H = hydrogen; A = acceptor.

Table 4: Magnetic and structural parameters of known dinuclear copper(II) complexes having half salen type ligands and double end on azide/cyanate bridges.

Complex (CCDC code)	Cu-N_{azide} (Å) (Short)	Cu-N_{azide} (Å) (Long)	Cu-N-Cu (°)	J (cm^{-1})	Reference
		Double $\mu_{1,1}$-N_3 complexes			
GOYPIV	2.009(2)	2.483(2)	88.68(6)	-2.28	24
YADGUG	1.999(1)	2.443(9)	88.3(4)	-2.63	25
IRIREG	1.998(3)	2.505(3)	89.2(1)	-8.5(5)	26
DEFQAH	1.990(9)	2.569(9)	90.6(3)	-4.2(2)	27
MUGFEA	2.012(4)	2.681(5)	99.4(2)	-146(5)	28
NIKHUM	1.984(18)	2.489(19)	87.7(7)	-10.16	29
NIKHOG	2.005(5)	2.500(5)	90.8(2)	-4.18	29
NIKLAW	1.983(5)	2.551(6)	84.3(2)	-1.43	29
JOPFIF	1.968(2)	2.404(2)	100.4(8)	-11.4	30
Complex 1	1.979(5)	2.442(5)	95.5(2)	-2.313	This Work
		Double $\mu_{1,1}$-NCO complexes			
GOYPUH	1.951(2)	2.528(2)	88.60(8)	-0.54	24
Complex 2	1.937(4)	2.692(4)	88.4(1)	0.513	This Work

Table 5: Mulliken spin densities (e) computed for the high spin (HS) configuration of complexes **1** and **2** and the low spin (LS) configuration of complex **1**.

Atom Label	1, High Spin	1, Low Spin	2, High Spin
Cu1, Cu1'	0.57	0.58, -0.58	0.57
O1,O1'	0.10	0.10, -0.10	0.10
N1,N1'	0.12	0.12, -0.12	0.12
N2,N2'	0.06	0.07,-0.07	0.06
N3,N3' (pseudohalide)	0.08	0.08, -0.08	0.08

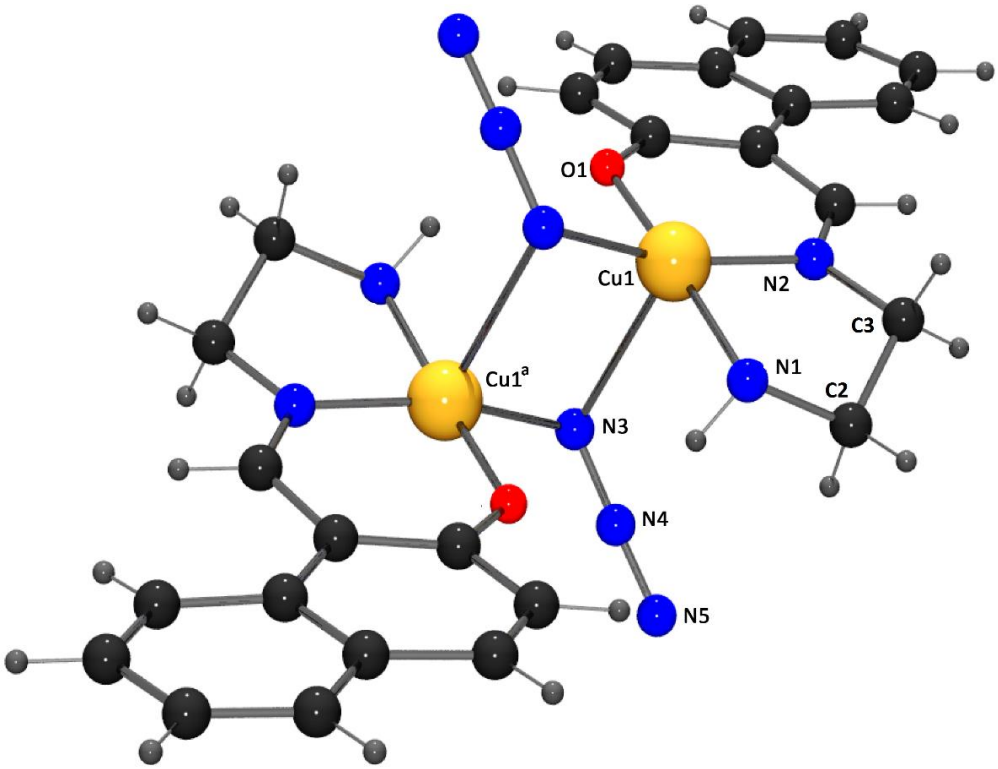

Figure 1: Perspective view of complex **1** with selective atom numbering scheme. Methyl groups of the amine nitrogen atoms have been omitted for clarity. Symmetry transformation: ª = -x,-y,1-z.

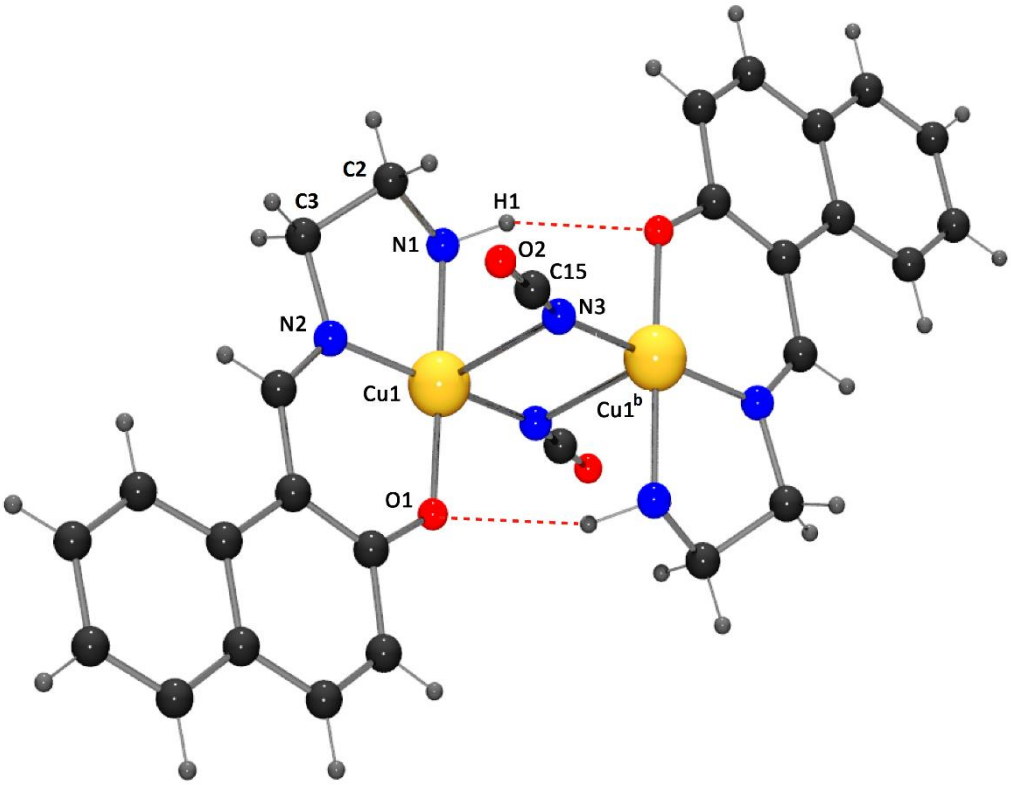

Figure 2: Perspective view of complex **2** highlighting the intra dimer hydrogen bonding interactions with selective atom numbering scheme. Methyl groups of the amine nitrogen atoms have been omitted for clarity. Symmetry transformation: ^{b} = 1-x,2-y,2-z.

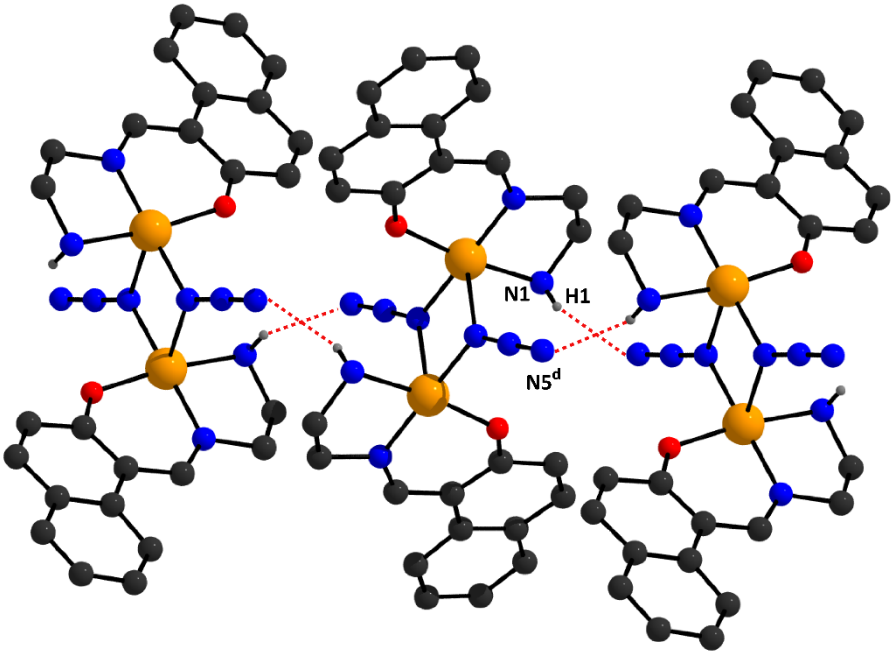

Figure 3: Hydrogen bonded chain of complex **1** showing only relevant atoms. Symmetry transformation: ^{d} = -x,-y,1-z.

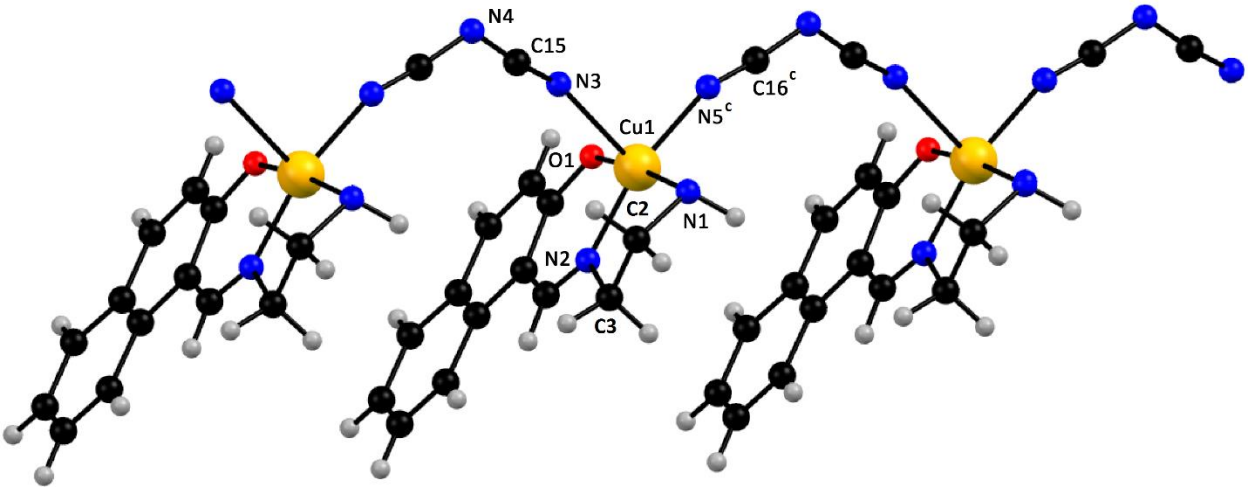

Figure 4: Perspective view of polymeric chain of complex **3** with selective atom numbering scheme. Methyl groups of the amine nitrogen atoms have been omitted for clarity. Symmetry transformation: ^{c} = -1+x,y,z.

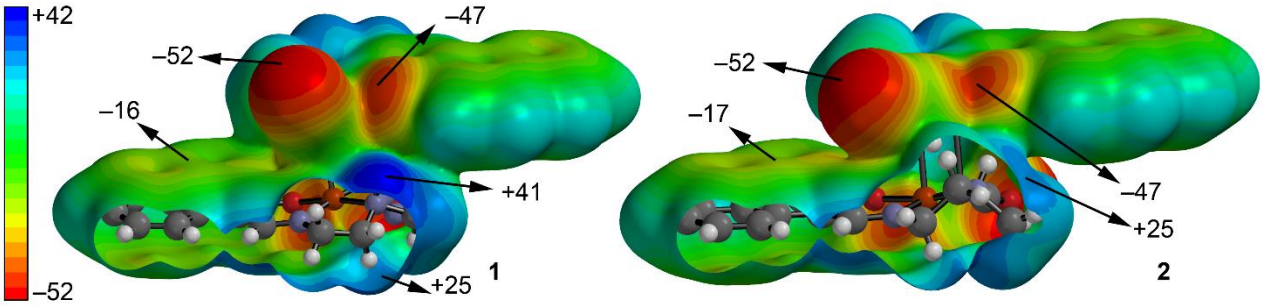

Figure 5: MEP surfaces of complexes **1** and **2**. MEP values in kcal/mol are given in selected points of the surface.

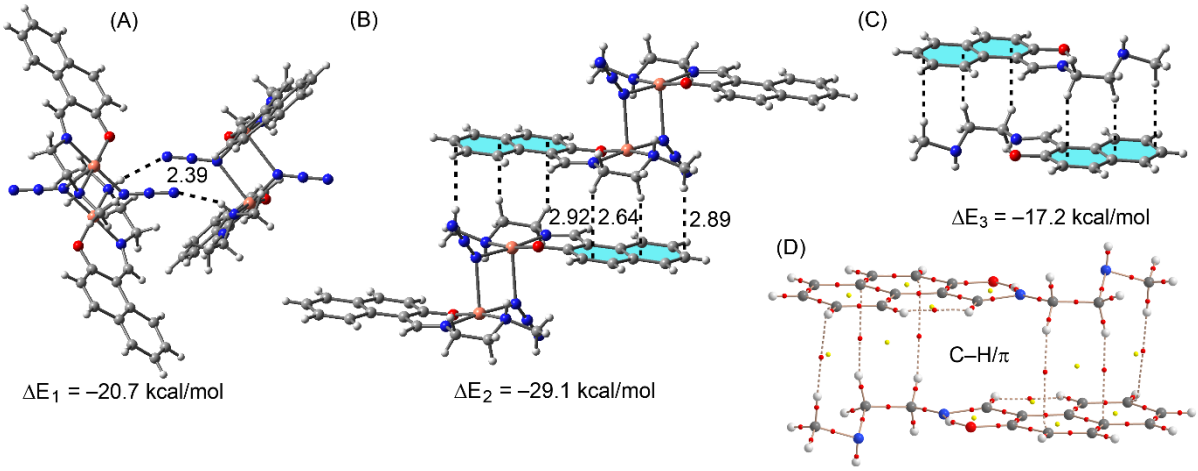

Figure 6: (A and B) Assemblies found in the solid state of **1**. (C) Theoretical model of the C-H···π complex without Cu. (D) AIM analysis of latter model. Bond and ring critical points are represented by red and yellow spheres, respectively. The bond paths connecting bond critical points are also represented by dashed lines. Distances in Å.

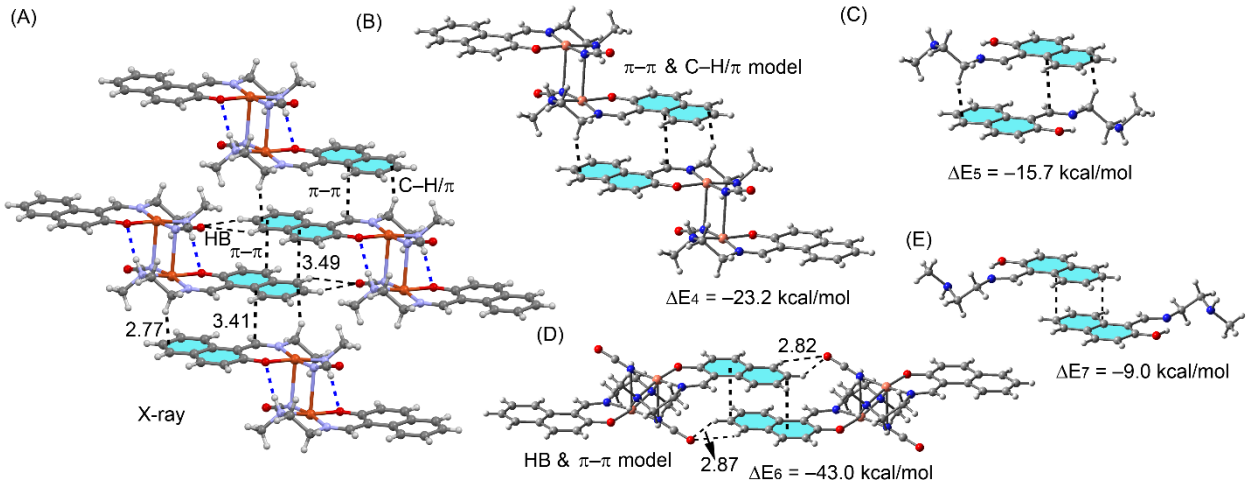

Figure 7: (A) X-ray fragment of complex **2**. (B-E) theoretical models used to evaluate the noncovalent interactions. Distances are in Å.

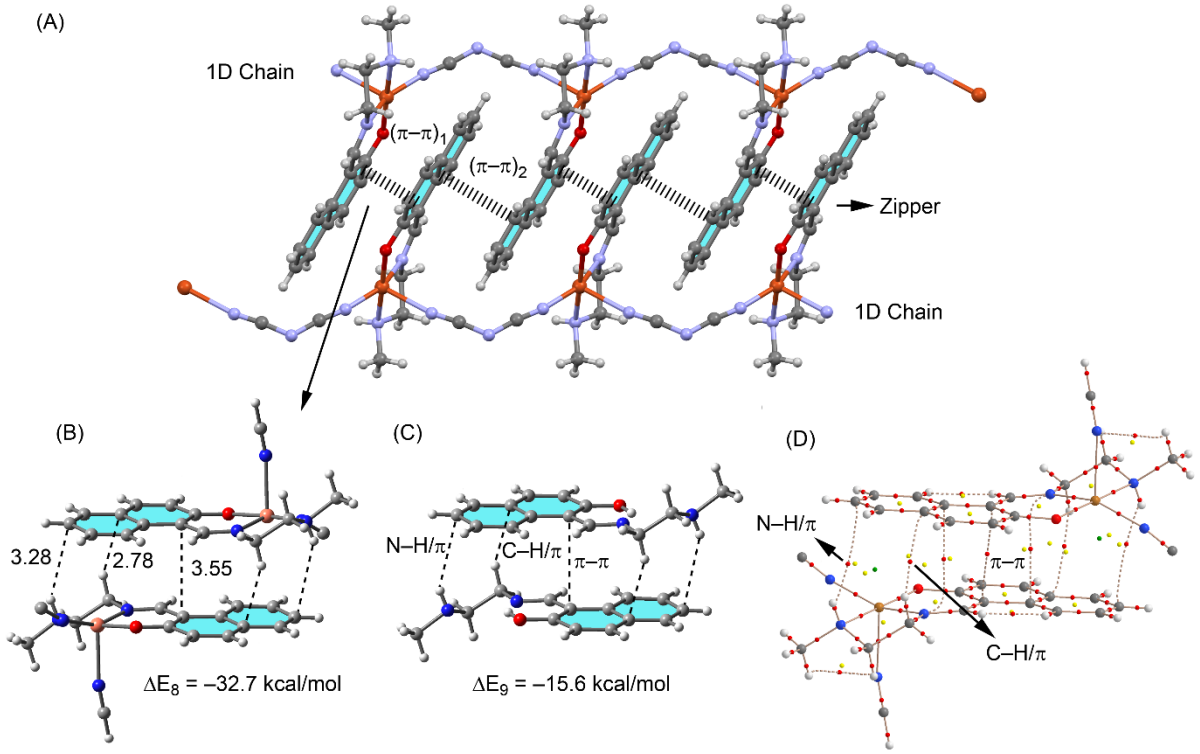

Figure 8: (*A*) Supramolecular zipper found in the solid state of **3**. (B and *C*) theoretical models of the $(\pi\cdots\pi)_1$ complex with and without Cu, respectively. (D) AIM analysis of model B. Bond, ring and cage critical points are represented by red, yellow and green spheres, respectively. The bond paths connecting bond critical points are also represented by dashed lines. Distances in Å.

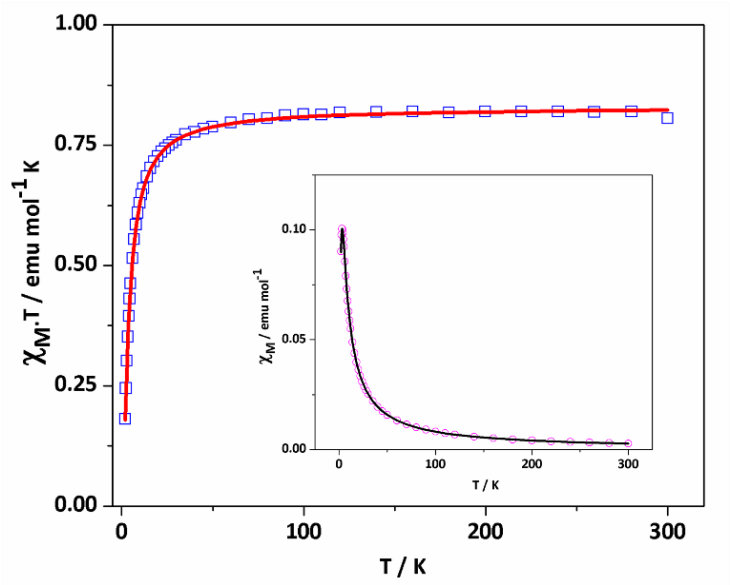

Figure 9: Plot of $\chi_M T$ vs T for a powder sample of complex **1** in a 1 T external magnetic field. Experimental data are shown as blue squares and the best fit is represented by the red line. Inset shows plot of χ_M vs T where the experimental data are shown as pink circles and the best fit is represented by the black line.

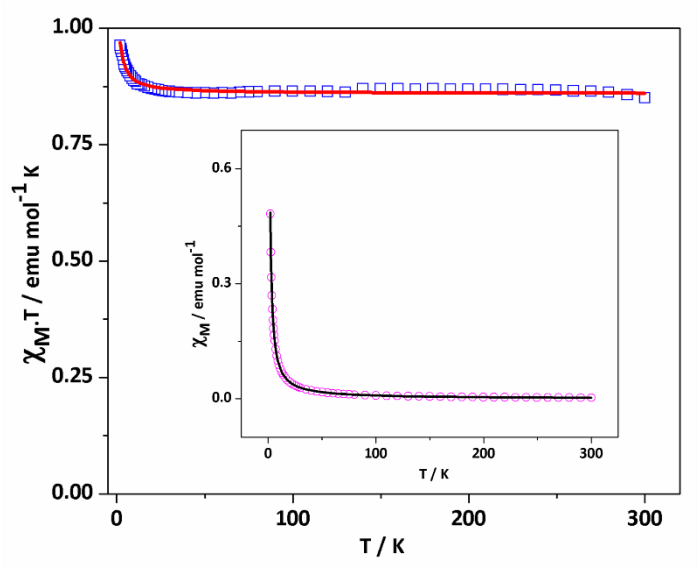

Figure 10: Plot of $\chi_M T$ vs T for a powder sample of complex **2** in a 1 T external magnetic field. Experimental data are shown as blue squares and the best fit is represented by the red line. Inset shows plot of χ_M vs T where the experimental data are shown as pink circles and the best fit is represented by the black line.

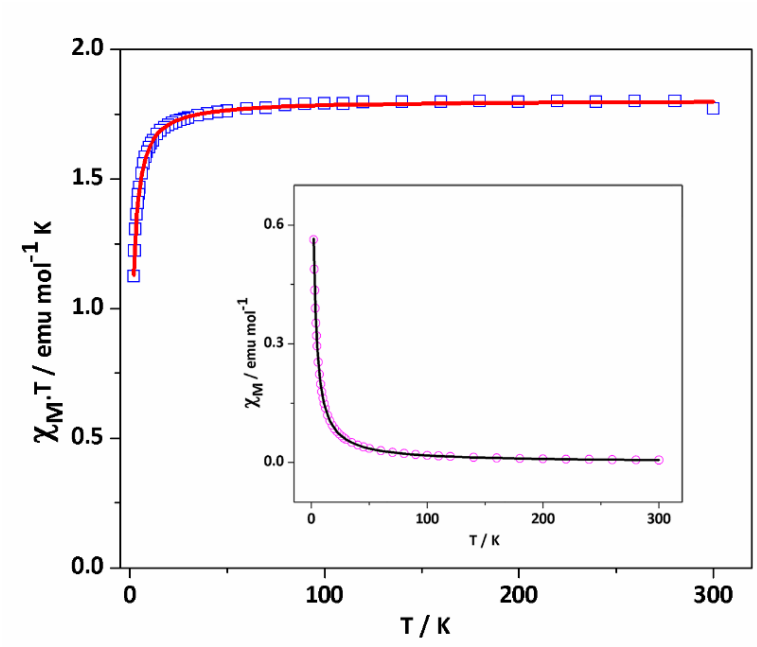

Figure 11: Plot of $\chi_M T$ vs T for a powder sample of complex **3** in a 1 T external magnetic field. Experimental data are shown as blue squares and the best fit is represented by the red line. Inset shows plot of χ_M vs T where the experimental data are shown as pink circles and the best fit is represented by the black line.

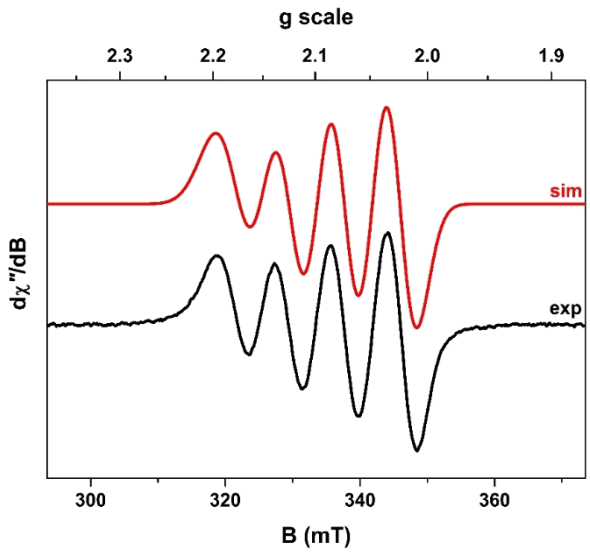

Figure 12: X-band EPR spectrum of complex **1** recorded in MeCN solution at 293 K (experimental conditions: frequency, 9.7976 GHz; power, 6.3 mW; modulation, 0.07 mT). Experimental data are represented by the black line; simulation is depicted by the red trace.

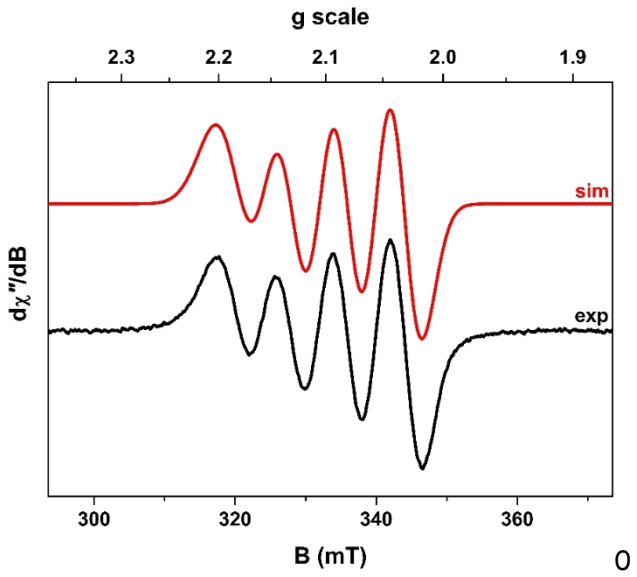

Figure 13: X-band EPR spectrum of complex **2** recorded in MeCN solution at 293 K (experimental conditions: frequency, 9.7826 GHz; power, 6.3 mW; modulation, 0.2 mT). Experimental data are represented by the black line; simulation is depicted by the red trace.

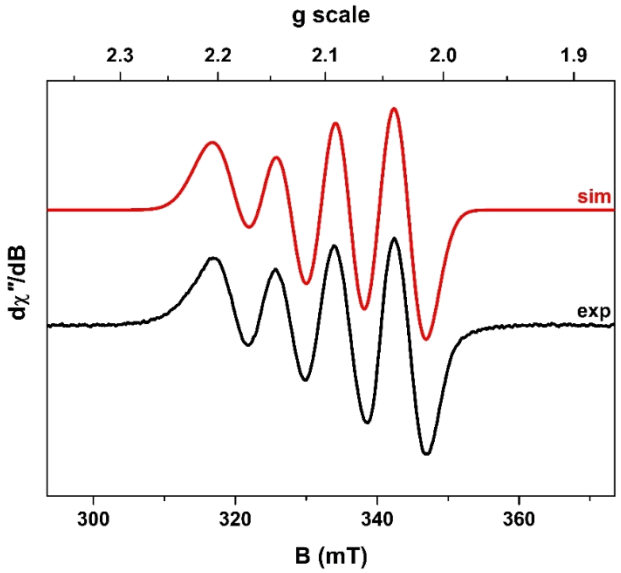

Figure 14: X-band EPR spectrum of complex **3** recorded in MeCN solution at 293 K (experimental conditions: frequency, 9.7786 GHz; power, 6.3 mW; modulation, 0.2 mT). Experimental data are represented by the black line; simulation is depicted by the red trace.

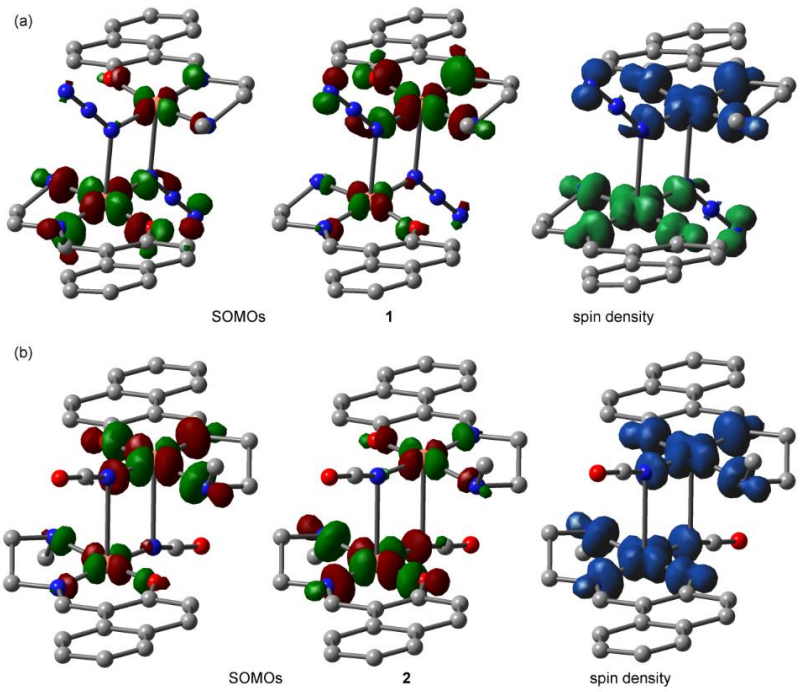

Figure 15: SOMOs of complexes **1** and **2** and their spin density plots (iso value = 0.004 e $Å^{-3}$).

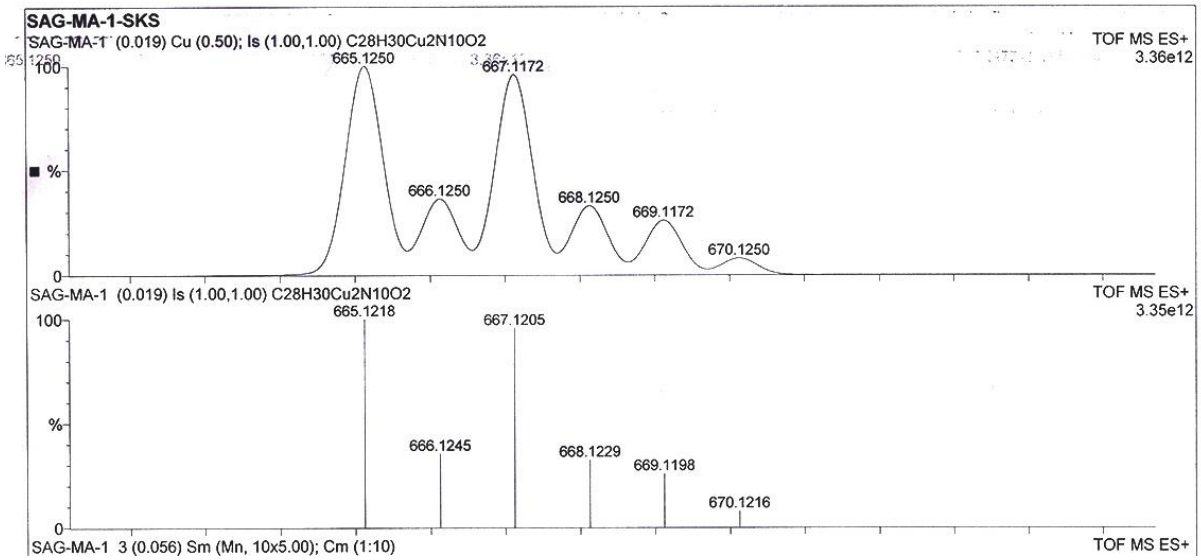

Figure 16: Part of the ESI-MS (positive) spectrum of complex **1** in acetonitrile showing the presence of $[\{Cu_2(L)_2(\mu_{1,1}\text{-}N_3)_2\}H]^+$ (m/z = 665.12) along with simulated isotopic distribution patterns.

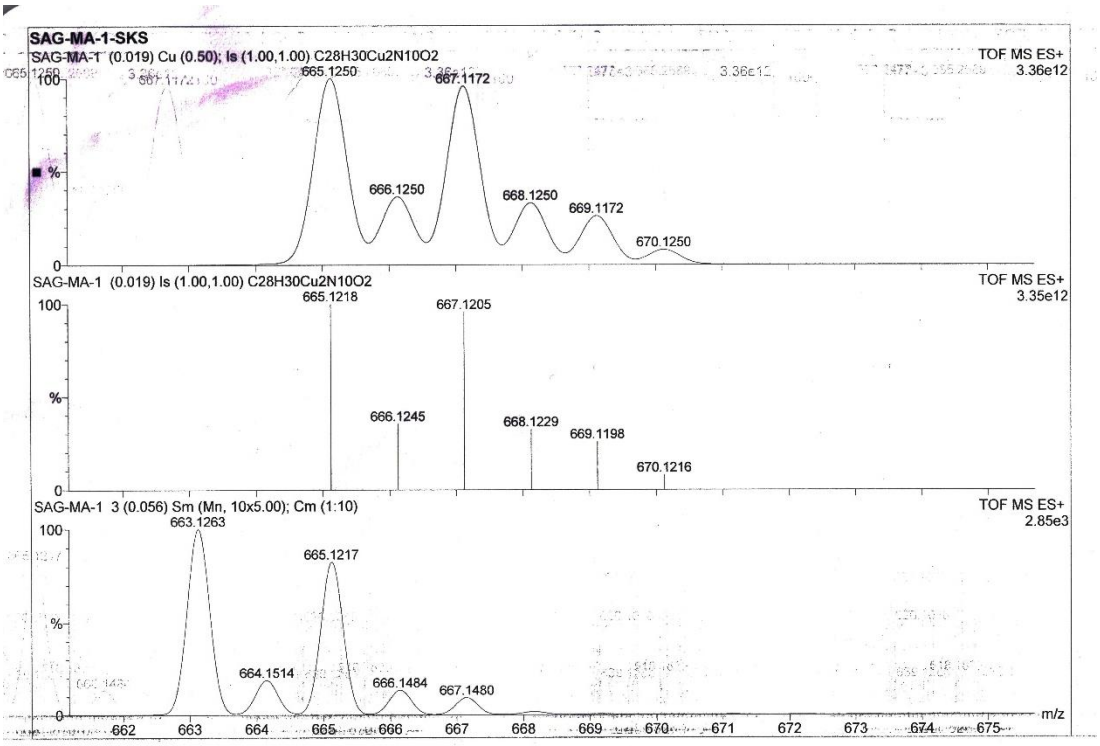

Figure 17: ESI-MS (positive) spectrum of complex **3** in acetonitrile showing the presence of the cation $[Cu_2L_2(dca)]^+$ (m/z = 645.96).

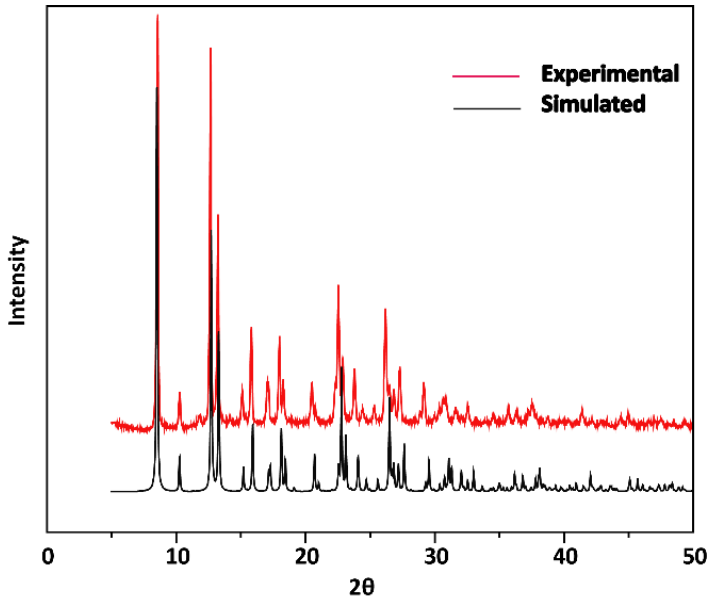

Figure 18: Experimental and simulated PXRD patterns of complex **1** confirming purity of the bulk material.

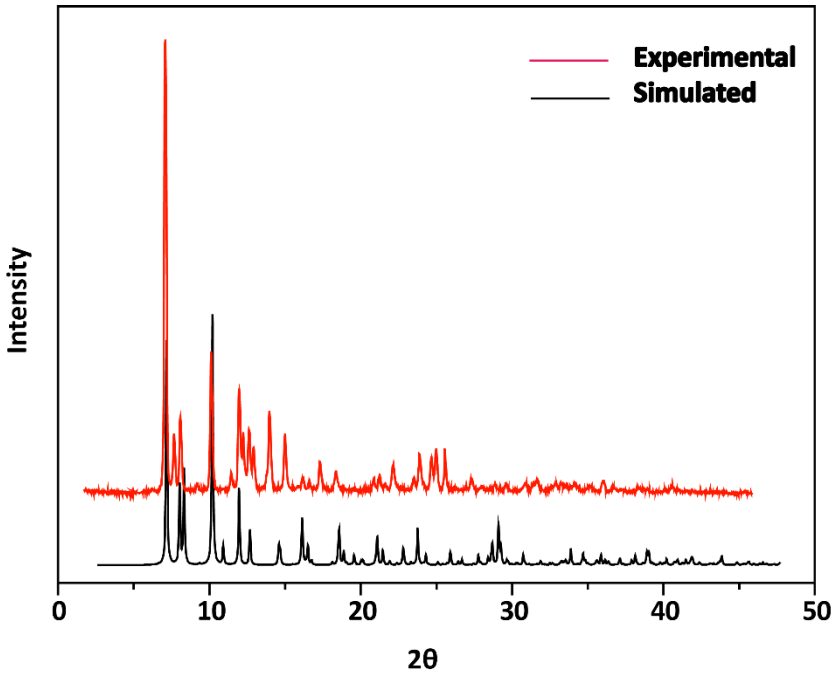

Figure 19: Experimental and simulated PXRD patterns of complex **2** confirming purity of the bulk material.

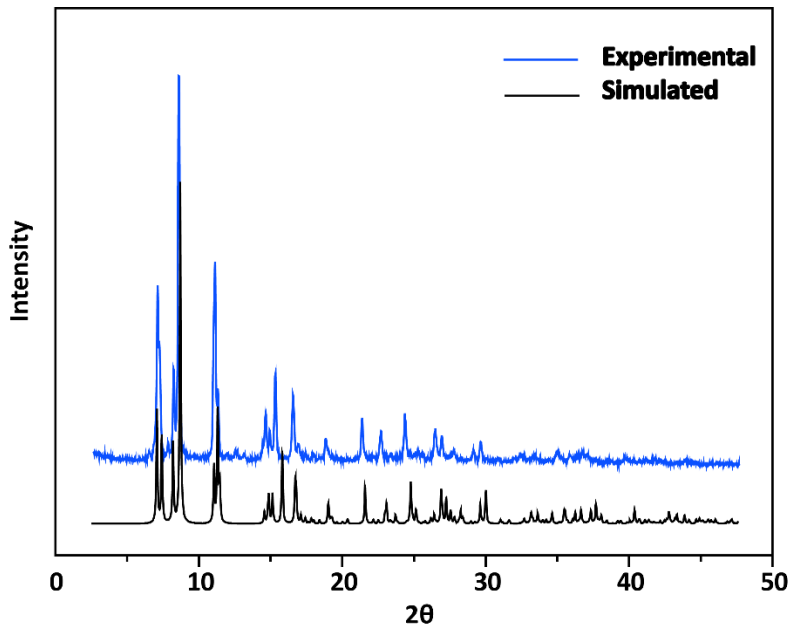

Figure 20: Experimental and simulated PXRD patterns of complex **3** confirming purity of the bulk material.

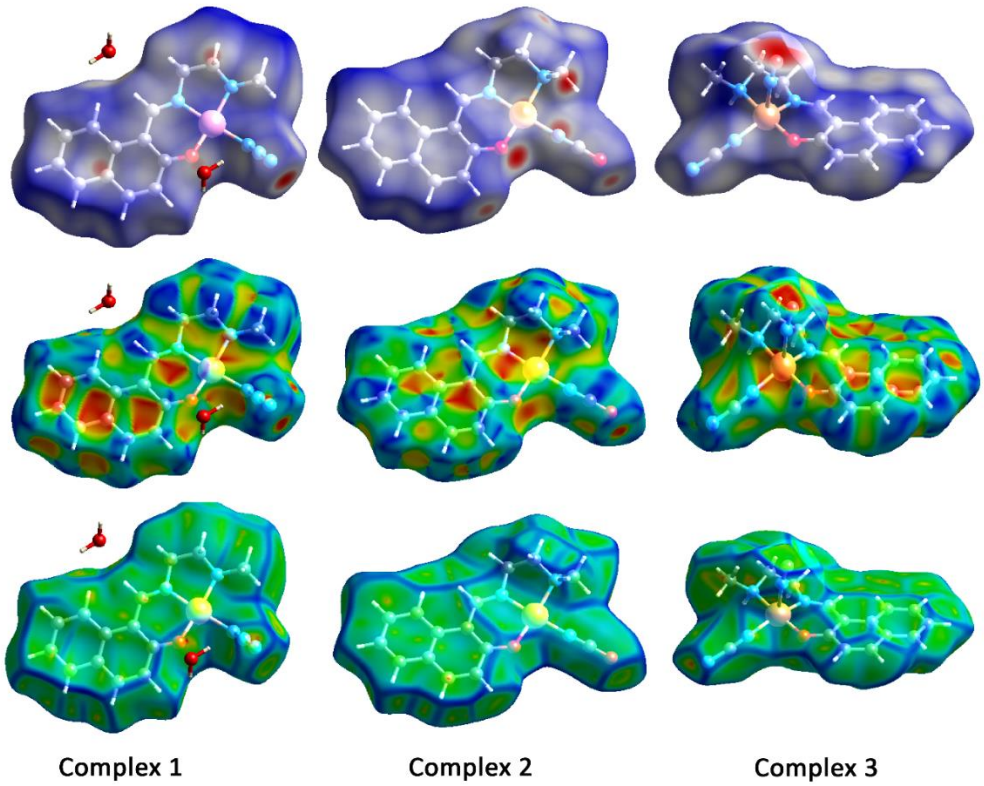

Figure 21: Hirshfeld surfaces mapped with d_{norm} (top), shape index (middle) and curvedness (bottom) for complexes **1**-**3**.

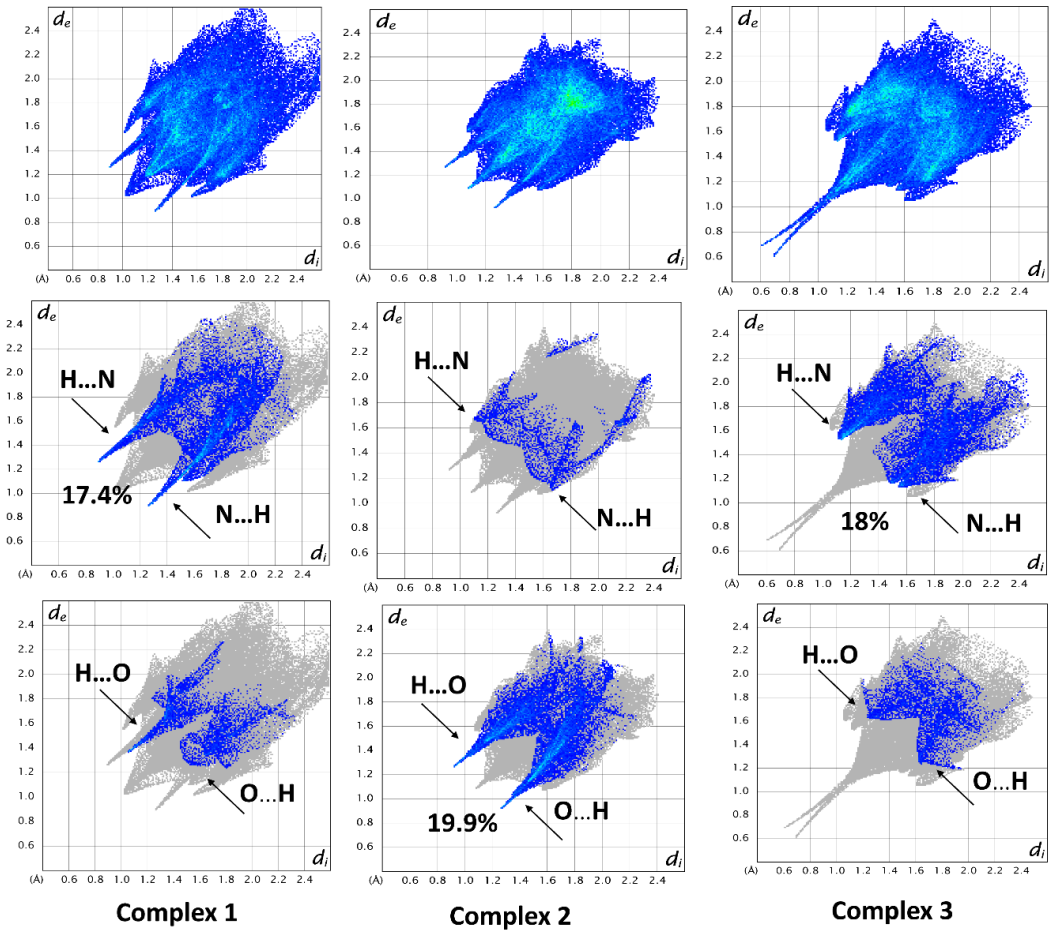

Figure 22: Fingerprint plot: Full (top); resolved into N···H/H···N (middle) and O···H/H···O (bottom) contacts contributed to the total Hirshfeld Surface area of complexes **1-3**.